



Review

Localized surface plasmon resonance: Nanostructures, bioassays and biosensing—A review

Eleonora Petryayeva, Ulrich J. Krull*

Chemical Sensors Group, Department of Chemical and Physical Sciences, University of Toronto Mississauga, Mississauga, Ontario, L5L 1C6, Canada

ARTICLE INFO

Article history:

Received 11 May 2011

Received in revised form 5 August 2011

Accepted 9 August 2011

Available online 1 September 2011

Keywords:

Localized surface plasmon resonance

Wavelength shift

Surface enhanced Raman spectroscopy

Metal enhanced fluorescence

Biosensor

Metal nanoparticle

ABSTRACT

Localized surface plasmon resonance (LSPR) is an optical phenomena generated by light when it interacts with conductive nanoparticles (NPs) that are smaller than the incident wavelength. As in surface plasmon resonance, the electric field of incident light can be deposited to collectively excite electrons of a conduction band, with the result being coherent localized plasmon oscillations with a resonant frequency that strongly depends on the composition, size, geometry, dielectric environment and separation distance of NPs. This review serves to describe the physical theory of LSPR formation at the surface of nanostructures, and the potential for this optical technology to serve as a basis for the development bioassays and biosensing of high sensitivity. The benefits and challenges associated with various experimental designs of nanoparticles and detection systems, as well as creative approaches that have been developed to improve sensitivity and limits of detection are highlighted using examples from the literature.

© 2011 Elsevier B.V. All rights reserved.



Eleonora Petryayeva is a graduate student under the supervision of Prof. Krull in the Department of Chemical and Physical Sciences at University of Toronto Mississauga. She holds a prestigious Canada Graduate Scholarship, and is pursuing studies in the area of coupling localized surface plasmon resonance with the optical properties of quantum dots for development of bioassays and biosensors.



Ulrich Krull is appointed as a Professor of Analytical Chemistry at the University of Toronto, and holds the endowed Astra Zeneca Chair in Biotechnology. His research interests are in the areas of biosensor and diagnostic technologies, and applications to biotechnology, forensic, clinical and environmental chemistry. His research work is exploring the use of nanoscale materials and microfluidics technologies to build devices for detection of DNA and RNA targets. Krull is an editor for *Analytica Chimica Acta*, and serves on a number of Scientific Advisory Boards for industry.

1. Introduction

Surface plasmons have attracted the attention of physicists, chemists, biologists and material scientists for widespread use in areas such as electronics, optical sensing, biomedicine, data storage and light generation. Recent developments in nanotechnology have generated new insights about control of various properties of nanomaterials that can support surface plasmons for specific

applications. Localized surface plasmon resonance (LSPR) is an optical phenomena generated by a light wave trapped within conductive nanoparticles (NPs) smaller than the wavelength of light. The phenomenon is a result of the interactions between the incident light and surface electrons in a conduction band [1]. This interaction produces coherent localized plasmon oscillations with a resonant frequency that strongly depends on the composition, size, geometry, dielectric environment and particle–particle separation distance of NPs. Common materials used for NP production are noble metals such as Ag and Au, which due to the energy levels of *d*–*d* transitions exhibit LSPR in the visible range of the spectrum [2]. Although, Ag exhibits the sharpest and strongest bands among all metals, Au is preferred for biological applications due to

* Corresponding author. Tel.: +1 905 828 5437; fax: +1 905 828 5425.
E-mail address: ulrich.krull@utoronto.ca (U.J. Krull).

its inert nature and biocompatibility [3], and thiol-gold association for immobilization of biomolecules.

The interaction of NPs with light allows some photons to be absorbed and some to be scattered. NPs undergoing LSPR can have high molar extinction coefficients for absorption, with magnitude of up to about $10^{11} \text{ M}^{-1} \text{ cm}^{-1}$, and Rayleigh scattering that can be many orders of magnitude larger than without LSPR [4,5]. For example, a single 80-nm Ag nanosphere has been reported to scatter 445 nm light with a cross-section of $3 \times 10^{-2} \mu\text{m}^2$. This is six orders of magnitude greater than the cross-section of capture of a fluorescein molecule, and three orders of magnitude greater than the cross-section of the nanosphere of the same size filled with fluorescein [6]. However, unlike fluorophores, plasmonic NPs do not photobleach or blink and thus can serve as intense and robust labels for biosensors, immunoassays, cellular imaging and surface-enhanced spectroscopies [7].

The extremely intense and highly localized electromagnetic (EM) fields induced by LSPR make NPs highly sensitive transducers of small changes in the local refractive index. These changes are exhibited in spectral shifts of extinction (absorption plus elastic light-scattering) and scattering spectra. For many organic molecules with a relatively high refractive index compared to solvent or air, binding to NPs results in a redshift. Additionally, strong EM fields enhance spectral information for surface-enhanced Raman spectroscopy (SERS), metal-enhanced fluorescence (MEF), plasmon resonance energy transfer (PRET) [7,8], and nanoplasmonic molecular rulers [9,10].

This review serves to describe the fundamentals of LSPR at the surface of conductive nanostructures, and offers examples from the literature to highlight applications in biosensing and bioassays where transduction of biorecognition events are typically based on LSPR wavelength shift, metal-enhanced fluorescence and SERS signals.

2. Origin of LSPR

The general optical properties of NPs differ significantly from those that are observed in bulk material. Metallic NPs that are of interest in this review have dimensions that place them in the quantum size regime. Continuous electron bands become discrete, and properties such as plasmon resonance will scale with NP size and the extent of aggregation of NPs. Upon plane-wave excitation of a small NP ($R/\lambda < 0.1$, where R is the radius of the NP and λ is the wavelength of the incident light), the oscillating electric field causes coherent oscillation of conduction electrons. This effect leads to the accumulation of polarization charges on the surface of a NP [1,6,11–13]. When only dipole oscillations contribute to the extinction cross-section, C_{ext} , Mie's solution of Maxwell's equation can be used to obtain the spectrum for well separated NPs [14,15]:

$$C_{\text{ext}} = \frac{24\pi^2 R^3 \varepsilon_m^{3/2} N}{\lambda \ln(10)} \frac{\varepsilon_i}{(\varepsilon_r + \chi \varepsilon_m)^2 + \varepsilon_i^2} \quad (1)$$

where ε_m is the dielectric constant of the surrounding medium, $\varepsilon = \varepsilon_r + i\varepsilon_i$ is the complex dielectric constant of the bulk metal, R is the radius of the NP and N is the electron density. The factor χ that appears in Eq. (1) accounts for the shape of the particle, and is assigned a magnitude of two for a spherical particle and can be as large as 20 for particles with high aspect ratios such as nanorods [16]. The surface plasmon resonance (Fröhlich frequency) peak that gives rise to the color of the spherical NP is observed when $\varepsilon_r = -2\varepsilon_m$. This represents a condition at which the EM field is enhanced, while polarization undergoes singularity as the denominator goes to zero. For Ag and Au NPs this condition is met in the visible region, making these materials suitable for numerous applications involving color. For ellipsoidal NPs, Richard Gans predicted

the splitting of surface plasmons into two distinct modes due to surface curvature and symmetry [17]. The extinction cross-section for NPs of various shapes can be theoretically modeled. For example, the value of C_{ext} for gold nanorods can be calculated as follows [17]:

$$C_{\text{ext}} = \frac{2\pi V}{3\lambda} \varepsilon_m^{3/2} \sum_j \frac{(1/P_j^2) \varepsilon_i}{(\varepsilon_r + (1 - P_j/P_j) \varepsilon_m)^2 + \varepsilon_i^2} \quad (2)$$

where V is volume of the particle and P_j is the depolarization factor. The depolarization factor for elongated particles is described as:

$$P_{\text{length}} = \frac{1 - e^2}{e^2} \left[\frac{1}{2e} \ln \left(\frac{1+e}{1-e} \right) - 1 \right] \quad (3)$$

$$P_{\text{width}} = \frac{1 - P_{\text{length}}}{2} \quad (4)$$

where e is ellipticity given by:

$$e^2 = 1 - \left(\frac{\text{length}}{\text{width}} \right)^{-2} \quad (5)$$

Therefore, ellipsoidal particles exhibit strong, polarization dependent spectra, where small changes in aspect ratio result in significant changes in extinction bands.

The oscillation of conduction electrons displaces the electron cloud relative to the nuclei, giving rise to a restoring force from coulombic attraction resulting in oscillation of the electron cloud with respect to the nuclei. This restoring force permits the resonance condition to occur at a specific frequency with electrons exhibiting a $\pi/2$ phase lag with respect to the field of incident radiation. The resonantly enhanced field inside the NP leads to the dipolar field that is exterior to the NP. It is the dipolar field that is responsible for enhanced absorption and scattering cross-sections, as well as strongly enhanced EM fields in close vicinity of the NP surface. A thin gold film (30–50 nm) absorbs throughout the visible and near-infrared region, while a dipolar surface plasmon resonance of a 30-nm Au NP is concentrated at 2.25 eV (ca. 552 nm) [12]. These collective oscillations of dipole plasmon resonance are governed by the shape and size of electron distribution, density of the electrons and effective electron mass [13]. For larger particles, modes with higher multipoles can occur (i.e. quadrupole) where half of the electron cloud moves parallel and half anti-parallel to the electric field [13]. A further factor known as the polarizability must be considered. The polarizability represents a distortion of the electron cloud in response to an external electric field and can be described as:

$$\alpha(\lambda) = 4\pi \varepsilon_m(\lambda) R^3 \frac{\varepsilon(\lambda) - \varepsilon_m(\lambda)}{\varepsilon(\lambda) + 2\varepsilon_m(\lambda)} \quad (6)$$

where maximum polarizability, α , is achieved when the absolute value of the denominator is at a minimum [18,19]. When the NP is coated with a thin layer of dielectric of thickness d and dielectric constant $\varepsilon_d(\lambda)$, the polarizability is defined as:

$$\alpha(\lambda) = 4\pi \varepsilon_m(\lambda) (R+d)^3 \frac{\varepsilon(\lambda) \varepsilon_A(\lambda) - \varepsilon_m(\lambda) \varepsilon_B(\lambda)}{\varepsilon_d(\lambda) \varepsilon_A(\lambda) + 2\varepsilon_m(\lambda) \varepsilon_B(\lambda)} \quad (7)$$

with

$$\varepsilon_A(\lambda) = \varepsilon(\lambda)(3 - 2P) + 2\varepsilon_d(\lambda)P \quad (7.1)$$

$$\varepsilon_B(\lambda) = \varepsilon(\lambda)P + \varepsilon_d(\lambda)(3 - P) \quad (7.2)$$

$$P = 1 - \left(\frac{R}{R+d} \right)^3 \quad (7.3)$$

The polarizability and internal polarization inside NPs are enhanced at the resonance condition as seen from Eq. (6). Spectral redshifts are observed with increasing dielectric constant of the environment, and result from the accumulation of polarization

charges on the dielectric that weakens the restoring force within NP. However, it should be noted that for larger particles that do not obey the Rayleigh approximation, the resonance red shift is a result of retardation effects where conduction electrons do not all move in phase [12]. The magnitude of the spectral shift of LSPR extinction, or the scattering wavelength maximum for small NPs is described by the following relationship [1]:

$$\Delta\lambda_{\max} = m\Delta n \left[1 - \exp\left(\frac{-2d}{l_d}\right) \right] \quad (8)$$

where m is the bulk refractive index response of the NP, also known as the sensitivity factor (in nm per refractive index unit, RIU), Δn is the change in refractive index (in RIU), d is the effective thickness of the adsorbed layer (in nm) and l_d is the characteristic EM field decay length (in nm). It is the expression given in Eq. (8) that serves as the foundation that explains the LSPR wavelength-shift (refractive index) arising in chemical assays and bioassays that probe the affinity between molecules at the surface of nanostructures.

2.1. Surface enhanced spectroscopic methods

Nanostructures that support plasmons play a significant role in enabling surface enhanced techniques, such as surface enhanced Raman spectroscopy (SERS) and surface/metal enhanced fluorescence (SEF or MEF). Raman scattering and fluorescence involve absorption and spontaneous emission. Scattering is instantaneous and fluorescence is typically a nanosecond scale multi-step process. In SERS, local field enhancement (absorption) and radiative (emission) contribute to the SERS cross-section. In MEF, fluorophores experience modified absorption cross-sections, while fluorescence intensity is governed by relative enhancements of radiative and non-radiative decay rates. Metal surfaces change radiative rates by amplifying the local photonic mode density and at the same time offer non-radiative pathways mainly through energy transfer to the metal. Thus, it is the relative magnitude of enhancement in decay rates that denotes the EM radiative efficiency, and this is a distinct difference between SERS and MEF. Quenching is observed at close fluorophore-NP distances where strong Raman enhancement dominates. As separation increases, fluorescence intensity reaches a maximum and then falls off [20], while Raman signal decays. Johansson et al. have proposed a general model of SERS and MEF using a theoretical analysis [21]. The following description of enhancement mechanisms is based on the SERS model.

In Raman processes only a small fraction representing about 10^{-6} of incident photons are scattered, making this technique at best suitable for structural analysis rather than sensitive trace analysis. On the contrary, SERS generates an enhanced Raman signal for molecules adsorbed to the surface of NPs or in the vicinity of “hot-spots”; spaces between NP arrays or aggregates (Fig. 1), or at the sharp edges or tips of individual NPs [22,23]. Two enhancement mechanisms are identified to account for this phenomenon: electromagnetic (EM) and chemical. The intensity of Raman scattering is proportional to the square of the induced dipole moment, which is a product of polarizability (chemical) and incident EM field intensity (electromagnetic). The so-called “EM factor”, is a result of coupling of EM fields (incident and scattered) with the SERS substrate. It is a local phenomenon and tends to influence molecules typically within a distance of ca. 10 nm. Concurrently, interaction of a molecule with a NP surface may lead to perturbations in electronic structure, thus inducing the change in polarizability.

The EM field is greatly enhanced under LSPR mode, and Raman scattering scales approximately with the fourth power of field enhancement. The electromagnetic mechanism is mediated from oscillations of surface conduction electrons of the NP resulting in an increased number of scattered photons. The signal inten-

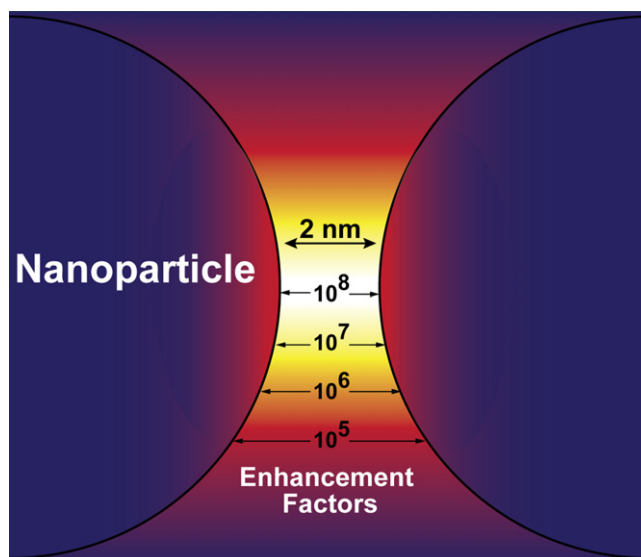


Fig. 1. An illustration of “hot spot” for NP dimer and rapid change in SERS enhancement factors with respect to relative position.

Adapted from Ref. [201].

sity in Raman spectroscopy is proportional to the cross-section of scatter, the intensity of the radiation source and the number density of molecules. The magnitude of enhancement in the cross-section of scatter is a function of roughness of the surface, and the chemical and optical properties of the adsorbed molecules. Interactions between the EM field of the conduction band of a NP and coulombic fields of an adsorbate results in a distortion of the molecule, resulting in the overlap of two electric fields and an increase in effective cross-section of scatter. At room temperature the distribution of molecules in vibrational energy levels is described by the Boltzmann distribution, indicating that the majority occupy the lowest energy level. This leads to notoriously low signals in the anti-Stokes shifts of Raman spectra. The enhancement of the anti-Stokes signal under LSPR mode was first described by Kneipp and coworkers who suggested an optical pumping mechanism [24]. The authors suggested that SERS can induce non-thermal populations of the first excited vibrational states of a molecule when in close vicinity of NP. However, further work by Haslett [25] and Brolo [26] indicated that high Stokes and anti-Stokes intensities arise due to modified cross-sections as a result of resonant or near-resonant excitation.

Significantly larger Raman signal enhancements are observed for NP aggregates in comparison to individual NPs [27–30]. As NPs are brought in close proximity with a separation much smaller than the wavelength of light, their transient dipoles couple and strong EM fields interfere coherently (i.e., “hot spot” regions). The spectral wavelength of NP aggregates tends to red shift, and the shift can reach near-infrared regions (NIR), providing potential for NP aggregates to be used for cellular and *in vivo* applications where tissue has minimal absorption [31,32].

Two important consequences of EM field enhancement are distance dependence and the excitation wavelength dependence of SERS. The enhanced EM fields extend well beyond the surface of the NP, thus creating a sensing volume of radius of some nanometers in which molecules can be detected. This implication is discussed in the following section in relation to the distance dependence of an analyte molecule to the NP. Maximum SERS enhancement tends to occur at an intermediate wavelength value between peak excitation wavelength and Raman vibrational frequency (wavelength). This results in simultaneous enhancement of incident and scattered photons.

Generally, very weak vibrational Raman modes with cross-sections in the range 10^{-31} to 10^{-29} cm² molecule⁻¹ can be enhanced by factors ranging from 10^4 to 10^{12} by placing a molecule in “hot-spots”. The SERS enhancement factor (EF) is strongly dependent on conditions such as excitation wavelength, NP substrate, and the analyte that is interrogated. The EF is commonly quantitatively described by Eq. (9) [1]:

$$EF_{SERS}(\omega_v) = \frac{|E_{out}(\omega)|^2 |E_{out}(\omega - \omega_v)|^2}{E_0^4} = \frac{I_{SERS}(\omega_v)/N_{surf}}{I_{NRS}(\omega_v)/N_{vol}} \quad (9)$$

where $E_{out}(\omega)$ is the incident excitation, and $E_{out}(\omega - \omega_v)$ is the resultant Stokes' shifted Raman signal. Experimental measurements of EF focus on interpretation of the right side of Eq. (9). The term $I_{SERS}(\omega_v)$ is the SERS enhanced Raman intensity, and is normalized by the number of molecules adsorbed to the NP (N_{surf}). This is compared in the form of a relative change by dividing the Raman intensity $I_{NRS}(\omega_v)$ with the number of molecules in the scattering volume, N_{vol} . This approach for estimation of EF presents some challenges with respect to practical applications due to the difficulty of accurate measurement of the number of molecules attached to a NP, as well as the notion of scattering volume and exact surface area of a NP. Other models to estimate average SERS substrate EF using experimentally measured signals have been proposed, with one example being [33]:

$$EF = \frac{I_{SERS}/(\mu_M \mu_S A_M)}{I_{RS}/(C_{RS} H_{eff})} \quad (10)$$

where I_{SERS} is the intensity of Raman signal, I_{RS} is the intensity of the Raman signal under non-SERS conditions, μ_M (m⁻²) is the surface density of NPs contributing to enhancement, μ_S (m⁻²) is the surface density of molecules adsorbed to NP, A_M (m²) is the surface area of metallic NPs, C_{RS} (M) is the concentration of the solution used for non-SERS measurements and H_{eff} (m) is the effective height of the scattering volume. A detailed description of EF has been thoroughly reviewed elsewhere [33], and due to its complexity is beyond the scope of this review.

While much is known about the EM based enhancement, the chemical mechanism is still a matter of a debate. The mechanism is often associated with a charge-transfer intermediate state formed upon coupling of the metal surface and a chemisorbed analyte molecule. This process in comparison to the EM field enhancement can be described as being even more distance dependent, and molecules directly in contact with the surface of the NP will significantly contribute to chemical enhancement. Therefore, this process is commonly referred to as *first layer effects* as molecules in this first layer exhibit stronger enhancement in comparison to those in adjacent layers [34]. The distortion of energy levels of molecules upon electronic interactions with metal orbitals leads to the shifts observed in Raman spectra as well as appearance of additional bands not characteristic of Raman.

3. Nanostructures

3.1. LSPR dependence on NP morphology, distance separation and proximity to NPs

The shape and size of metallic NPs contribute to spectral properties due to the changes in surface polarization. Various shapes such as spheres, triangles, cubes, prisms, bipyramids, octahedrons, nanorods, nanoshells, nanostars as well as structured array films have been synthesized to tailor LSPR absorption from visible to infrared regions. An increase in edges or sharpness of a NP results in a red shift of extinction spectra due to an increase in charge separation, while increased symmetry results in increases of LSPR intensity [3]. The number of resonance absorption peaks is deter-

mined by the number of modes in which a given NP can be polarized [2,3,15]. Thus, nonspherical NPs tend to exhibit multiple, red-shifted peaks in comparison to spherical particles, as illustrated by Fig. 2. For example, nanorods that can be polarized along two axis, transverse and longitudinal exhibit two LSPR peaks in agreement with Eq. (2). The size of the NPs influences the relative magnitude of the absorption cross-section and the cross-section of scatter. For NPs smaller than 20 nm, the predominant process is absorption. An increase in physical dimensions or effective size of NPs increases the cross-section of scatter. This relationship is usually expressed as a ratio of scattering to absorption, and while dependent on size this relationship tends to be independent of the aspect ratio of the NPs [35].

Spectral shifts associated with LSPR of NPs are influenced to a greater extent by deviation from spherical geometry than by an increase in size. For instance, changing the size from 10 to 100 nm for spherical NP results in a red shift of 47 nm, while change in aspect ratio from 2.5 to 3.5 for an elliptical NP results in shifts of the longitudinal band by 92 nm [2]. In this example, the change of aspect ratio correlated to a much smaller change in the overall size of the NP. The refractive index sensitivities also tend to depend on the shape of the NP, with the highest observed for nanorods, followed by triangles and then spheres [36].

The key interest in selection of various shapes is to create “hot-spot” regions. Concurrently, there is some trade-off in the width of an LSPR peak, as this typically increases as the sharpness of a tip or edge increases [37]. The physical coupling of these two parameters is a manifestation of the “lightning rod effect”, explained as a “roughness-induced momentum matching of surface plasmons to the radiation field” [37]. This effect causes the dipolar fields of NP to be concentrated at the tip of the NPs, which leads to enhanced electric fields crucial for surface enhanced spectroscopies. For a detailed physical description of this phenomenon the reader is referred to the article by Gersten and Nitzan [38].

The dielectric sensitivity of the NP is dependent on the spectral position of LSPR, as well as geometric parameters. The refractive index sensitivity was reported for a single silver triangular nanoprism, with a spectral shift of 4.4 nm per each additional CH₂ unit on linear alkylthiol [37], a modest 0.7 nm for hole array in gold film [39] and 5.2 nm for gold nanorings [40]. A systematic study has focused on understanding the relationship between morphology and LSPR. This work used an array of silver triangles on an indium tin oxide film. Cycles of chronocoulometric electrochemical treatment induced morphological changes to NPs in a controlled manner through selective oxidation [41]. At first the bottom edges of the triangles became more rounded in shape, followed by rounding of the triangular tips and finally the top face of the triangles eroded resulting in reduction of the height of NPs. Each step resulted in a blueshift of λ_{max} allowing for direct correlation between LSPR response and geometrical changes.

The dependence of LSPR response on the separation distance between NP and adsorbate is described by the electromagnetic field decay length. Generally, it is assumed to be an exponential decay as shown in Eq. (8). However, Eq. (8) does not specifically take into account the shape of the NP and the effect that this imposes on the EM field. The distance dependence, d of SERS intensity found from Mie theory for a sphere of radius, a , is defined as $1/(a+d)^{-12}$, given that the EM field enhancement decays with a^{-3} and that there is a fourth power EM enhancement. However, in practice it was found that enhancement extends to ca. 10 nm from the surface of the NP and the distance at which SERS intensity drops by a factor of 10 is ca. 2.8 nm [42]. Therefore, the enhancement is a long-range effect and extends beyond a monolayer regime. A study that examined the relationship experimentally used a pyridine molecule and a NP coated by alumina layers of various thicknesses. The alumina layer that served as a spacer between the NP and pyridine revealed the

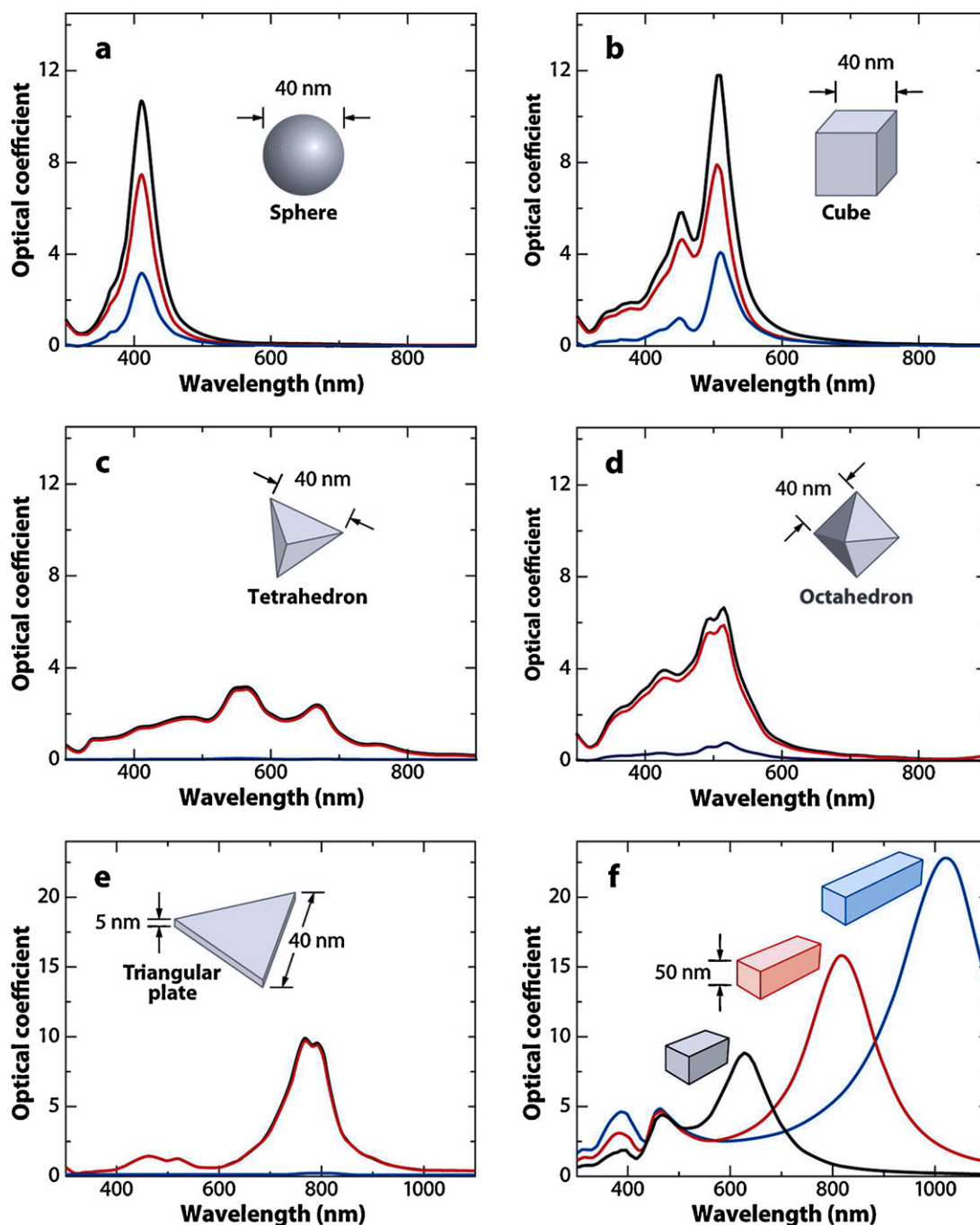


Fig. 2. Extinction (black), absorption (red), and scattering (blue) spectra calculated for Ag nanoparticles of different shapes: (a) a sphere displaying a single dipole resonance peak and (b) a cube, (c) a tetrahedron, (d) an octahedron, and (e) a triangular plate. (f) Extinction spectra of rectangular bars with aspect ratios of 2 (black), 3 (red), and 4 (blue). Note that the nonspherical particles typically exhibit multiple, red-shifted resonance peaks. (For interpretation of the references to color in the figure caption, the reader is referred to the web version of the article.)

Reprinted with permission from Ref. [3].

following relationship for Raman intensity, I , by fitting experimental data [1]:

$$I = \left(1 + \frac{d}{a}\right)^{-10} \quad (11)$$

where a is the size of the NP and d is the separation distance. This equation considers that at increased distances the surface area is also increased, scaling with a^2 .

The proximity of NPs to each other, particularly when arrayed onto substrates is another factor that can be used to control LSPR effects. The spectra of interacting particles in a dimer or an aggre-

gate exhibit red shifts and the appearance of a lower energy absorption band. A decrease in gap distance between NPs results in an increase in SERS enhancement. Two primary processes are used to describe EM interactions based on the spacing. The near-field dipolar interactions prevail when two NPs are placed such that the separation is much smaller than wavelength of light. The far-field dipolar interactions dominate when spacing is on the order of the wavelength. The far-field interaction is a dynamic process, as a dipole field in one NP induces oscillations in an adjacent NP. Examples of the effects of inter-particle distance on spectral position of the extinction band and plasmon decay time was

quantified by Lamprecht et al., using a square array of 150 nm Au NPs [43].

3.2. Fabrication of nanostructures for LSPR

Nanofabrication techniques are classified into top-down and bottom-up methods, where the latter is successfully used for the self-assembled synthesis of semiconductor quantum dots, while the synthesis of Au and Ag nanostructures is primarily based on top-down approaches.

3.2.1. Wet chemical reduction method

Noble metals crystallize in face-centred cubic lattices, and single crystal NPs form a truncated octahedron structure, also known as a Wulff polyhedron [3]. The presence of surfactants and stabilizing agents in a reaction mixture allows for generation of different shapes. Numerous methods have been reported in the literature, and reproducible procedures for controlled shape and morphology of NPs tend to rely on seed-mediated synthesis [22]. The number of twinning defects or stacking faults within the initial seed pre-determines the final structure of the NP [3]. These defects allow for preferential growth directions, as they produce more reactive sites for heterogeneous nucleation. For instance, a single crystal seed can grow into an octahedron or cube, which by activation of specific sites using oxidative etching can ultimately be used to grow nanorods and nanobars (Fig. 3a) [3].

In general terms, nanoparticle production is a two-step process: first, rapid nucleation of metal nuclei is produced by reduction of a precursor to form seed particles with a size range of 1–5 nm [44]. Small seed particles are obtained under conditions of high precursor concentration. The second step is the growth of the NP; a slow process achieved with addition of more metal ions and often a different reducing agent. The classical method for the synthesis of gold NPs is based on the reduction of gold chloride with sodium citrate in hot aqueous solution. Ag NPs are commonly synthesized using

AgNO₃ with NaBH₄ or sodium citrate. Versatile methods based on such chemistry have been described where ethylene glycol served simultaneously as solvent and reducing agent. A capping agent such as poly(vinyl pyrrolidone) (PVP) is then added to selectively bind to the {100} facets, while citrate ions bind to {111} facets, allowing for the dominance of growth of a particular crystal facet. It has been shown that kinetic rates of lateral and vertical growth are dependent on the capping agent. Vertical deposition is favorable with PVP agent, while lateral deposition was seventy times faster in the presence of citrate [45]. The cationic surfactant, cetyltrimethylammonium bromide (CTAB) has been useful in preparation of a variety of geometries of Ag and Au NPs due to its selective adsorption to the {111} facet of the seed [46]. It should be noted that impurities in CTAB play a key role in the synthesis of nanorods [47]. A multitude of synthetic methods for the preparation of Au, Ag, alloy Ag/Au and core/shell Au/Ag NPs have been described in the literature [3,44,48–55], as well as approaches to control the morphologies and growth mechanisms of NPs [44].

3.2.2. Lithography and vapor deposition

Vapor deposition techniques are extensively used to generate ultrathin metallic nanoislands. Vacuum deposition or sputtering is based on evaporating a metal and then condensing the metal atoms. Thicknesses less than 10 nm for a film with defined island structure are obtained and monitored using a quartz crystal microbalance. Nanopatterned structures, including periodic particle arrays (PPAs), nanoholes and dimers are prepared using lithographic methods [56,57].

Numerous lithographic techniques have been used to achieve size and shape control of nanostructures. Electron beam (EB) lithography allows for precise control of size, shape and spatial distribution, generating greater than 99% monodisperse populations of NPs owing to high resolution (less than 100 nm) [58,59]. An electron sensitive photoresist, such as poly(methyl methacrylate), PMMA is coated over a glass slide that supports a conductive film

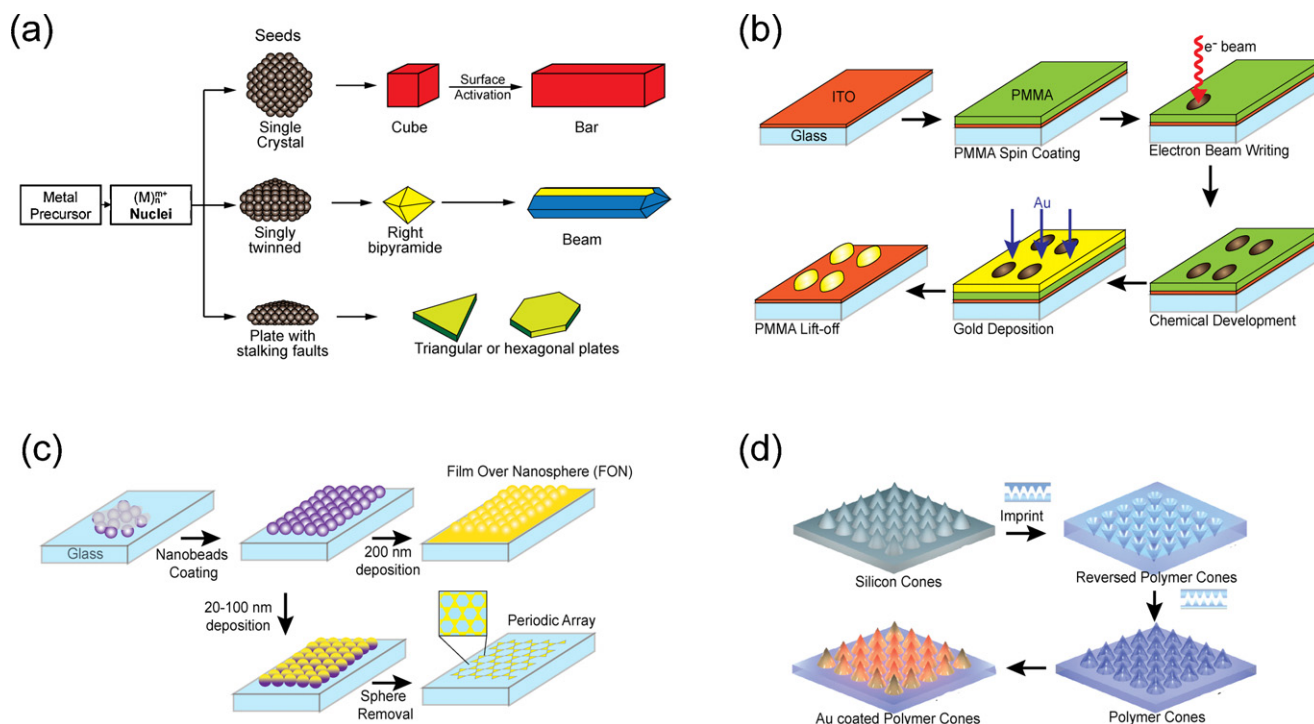


Fig. 3. Nanofabrication techniques. (a) Wet seed-mediated chemical reduction method for synthesis of NPs of various shapes; (b) principle of EB technique; (c) nanosphere lithography process used to generate FON with 200 nm thickness Au deposition and NP arrays when 20–100 nm Au is deposited on the surface; (d) schematic of the nanofabrication process for 3D Au coated nanocones by nanoimprint lithography. Reprinted with permission from Ref. [44], doi:10.1088/0957-4484/21/25/255502.

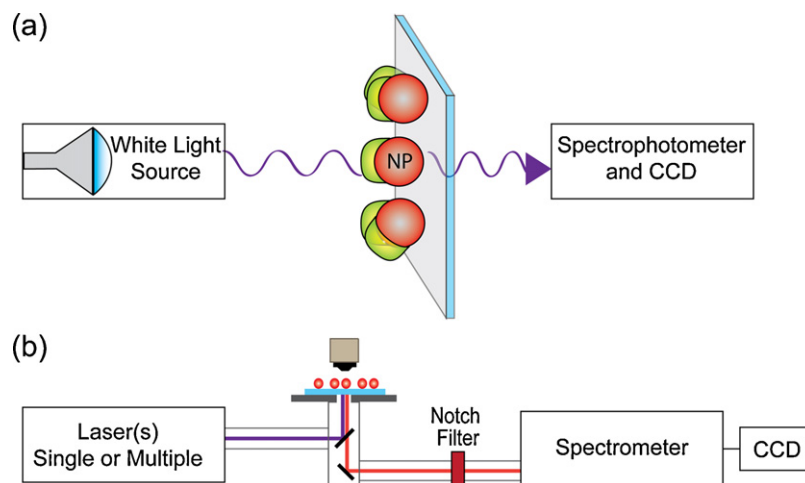


Fig. 4. Schematic diagram for instrumentation used in LSPR. (a) Transmission geometry for measurement of extinction spectrum of NPs. (b) SERS detection using epi-illumination set-up equipped with multiwavelength laser excitation system, x - y transitional stage and spectrometer along with notch filter to remove Raileigh scattering. Detection is achieved with CCD.

such as indium tin oxide (ITO). The electron beam is then used to burn off the polymer in a desired pattern and the exposed surface is chemically developed. Gold or silver is deposited by thermal evaporation at a rate $1\text{--}2\text{ nm s}^{-1}$ and finally PMMA is removed by acetone, leaving behind the desired pattern [60]. This technique (Fig. 3b), as well as focused ion beam lithography remain time consuming, and produce only small patterned regions at one time (typically about $100\text{ }\mu\text{m} \times 100\text{ }\mu\text{m}$) [58].

An alternative cost-effective technique is nanosphere lithography (NSL), which produces 2D periodic arrays and metal films-over-nanosphere (FON) structures. Due to substantial roughness, the FON structures are extremely efficient SERS substrates. The NSL process illustrated in Fig. 3c is based on the self-assembly of polymer nanospheres arranged in a close-packed hexagonal pattern that is subsequently overcoated with metal [61]. Metal deposited over the mask with a thickness between 15 and 100 nm generates honeycomb lattices of triangular islands once the mask is washed away. The dimensions of these islands can be controlled by the gap size between spheres, and is dependent on the initial bead size [62]. Nanosphere masks formed by polystyrene nanospheres upon solvent evaporation are prone to defects as a result of size dispersity, point defects (missing nanospheres), line defects (nanosphere slips), and the randomness of arrangement. The typical defect free regions are spatially distributed across distances between 10 and $100\text{ }\mu\text{m}$ [11]. Angle-resolved NSL, also known as shadow NSL, uses annealed polystyrene spheres to expand the range of accessible NP morphologies to include nanodisks, nanorings, nanoholes and cup-like structures [62].

Nanoimprint lithography (NIL) is considered to be a next generation lithographic technique that offers high precision comparable to EB lithography, while offering high throughput suitable for large-scale patterning [58]. Unlike traditional lithographic techniques that rely on modifications of a resist over coating as induced by photons or electrons, NIL is based on the mechanical molding of polymer material [63]. The resolution of this technique is not limited by the wavelength of a radiation source, and the smallest achievable dimensions are defined by fabrication of an imprinting stamp. Soft lithography was successfully used to generate arrays of nanoholes and nanoparticles [64]. As one example, SERS active substrates produced by Wu et al. were composed of Au coated nanocones (Fig. 3d) [65]. These 3D nanostructures had tip radii less than 10 nm, providing for efficient EM field enhancement and an estimated SERS limit of detection of 0.3 zeptomoles of 1,2-bis(4-pyridyl)-ethylene (BPE) [65].

Among other nanofabrication techniques are laser ablation, based on photo- and radiolytic reduction of metal ions, electrodeposition and variations of lithographic techniques (electrostatic colloidal and soft interference). An interesting example of an electrochemical deposition technique was reported by Bok et al. to prepare Au/Ag alloy nanorods with multipole LSPR modes. The tunability of the resonance wavelength was achieved by varying proportional composition of two noble metals in a plating solution [66].

It has been observed that isolated holes in a conductive film can be induced to support surface plasmons resulting in transmission of light through the film where the transmission can be modified by plasmonics [67]. A much greater optical effect is seen for periodic arrays of isolated holes in metal films. These can support an extended LSPR if the holes are of a size that is smaller than the wavelength of incident light, and each hole as a point source is within the decay length of surface plasmons such that the plasmons can overlap and interact [68].

Physically, it is the spatial periodicity of the dielectric constant and the presence of conductive metal that serves to create surface plasmon polariton Bloch waves (SPP-BWs). Such Bloch waves influence dispersion of light, and can be interpreted to be associated with formation of a band gap [69].

Periodic arrays can take the form of a single set of linearly positioned structures in metal films, or two-dimensional arrays of nanoholes. Nanohole structures have been investigated to determine the effect of size, shape, density and periodicity [70–76]. Generally, a similar spectral outcome is observed whether the geometry of a hole is square or round. Larger holes can transmit more light up to a size of about 200 nm diameter.

Optimization of the design of nanohole structures addresses both the intensity of optical transmission and the wavelength of the main transmission peak. For example, a repeating separation distance of about 600 nm for holes of 200 nm size will result in transmission of optical radiation at about 700 nm in ambient atmospheric conditions. As observed for periodic structures based on metal islands, a change in local dielectric constant can lead to a shift of wavelength [77,78]. The sensitivity of nanohole arrays is typically about 200–300 nm for each full unit of refractive index.

Common methods that are used to prepare nanohole arrays make use of either top down techniques such as electron beam lithography and focused ion beam milling, or a hybrid bottom up/top down approach that relies on self-assembled diblock copolymer structures that are selectively etched for use as templates

for metal deposition [79]. At present, focused ion beam milling is the method of choice in terms of reliability and reproducibility [80].

4. Instrumentation

LSPR instruments are typically built in-house and are designed to handle a particular experiment or application. In general, they consist of three main components: a light source (white light or laser), the sample and a detector. Among common detection techniques are ultraviolet–visible (UV–vis) spectroscopy, dark-field scattering microscopy, SERS and SEF measurements. The extinction spectrum of the NPs is measured using UV–vis spectroscopy with excitation relying on a white light source. For transparent samples, light is passed directly through the sample (Fig. 4a). For non-transparent samples such as encountered using FON substrates, an optical geometry suitable to study reflection is used.

Imaging is achieved with dark-field microscopy where small regions, as well as single nanoparticles are studied. The incident white light strikes the surface at a high angle and scattered light is collected at the low angle. A two-aperture set-up would rely on a high numerical aperture objective lens to bring incident light obliquely to a surface, and an objective selected for suitable numerical aperture would be used to collect the scattered light. A dark field objective can also be used in reflection mode where incident and collected light travel through the same objective. The scattered light is then sent to the spectrometer and detector, where the most common imaging detector is a camera that uses a CCD chip.

A laser light source is typically used for SERS experiments, and Raman scattered light is collected and processed using a combination of holographic notch filter with a spectrograph to isolate energy bands of scattered radiation. The orientation of incident radiation with respect to the sample is typically either at a glancing angle, or can be associated with an epi-illumination microscope configuration (Fig. 4b). Raman (SERS) mapping is achieved with a CCD, while raster-scanning (point mapping) with xy-translational stage generates 2D spectra-based image. Inclusion of multiple wavelength light sources leads to hyper-spectral SERS imaging. The image is presented as a 3D cube, where two (*x* and *y*) dimensions define the pixilated area and the third is the spectral dimension of wavelength.

5. Applications

LSPR offers a platform for biological and chemical sensing that typically relies on one or more of the following mechanisms: (1)

resonant Rayleigh scattering, (2) charge–transfer interactions at the surface of the NP, (3) NP aggregation, and (4) changes in local refractive index. In addition, LSPR is widely used to enhance surface optically related processes such as fluorescence, plasmon resonance energy transfer (PRET) and SERS.

The design of sensing platforms that use NPs requires functionalization, bioconjugation and often immobilization of NPs. Strategies for immobilization typically involve physisorption, self-assembly or covalent bond formation. Gold NPs are often modified with thiol or disulfide-terminated molecules to displace stabilizing ligands used during NP synthesis (e.g. CTAB, citrate). Functionalization of Ag NPs can be challenging, as they are susceptible to oxidation and etching by chloride ions. Although Ag NPs can be immobilized on amine-functionalized substrates, amines affect the colloidal stability of NPs promoting air oxidation [81]. To overcome these challenges NPs are coated with a SAM, such as mercaptoundecanoic acid, or are encapsulated with a thick silica shell, where the latter leads to significant increase in size [81]. Coating of Ag nanoprism edges with a protective layer of gold provides NPs that are resistant to chloride etching [82]. An extensive survey of bioconjugation methods used to create NP-bioconjugates can be found elsewhere [83,84].

5.1. Transduction with LSPR wavelength-shift

The high sensitivity of LSPR to the dielectric environment is advantageous for detection of molecular binding events and conformational changes, and can provide steady-state and kinetic data. The LSPR spectral shift has been implemented as a transduction strategy to investigate binding interactions of a variety of biological and pathogenic molecules in a label-free approach. A comparison of analytical performance of LSPR and SPR sensors (Kretschmann configuration, fiber optic, grating coupling) can be found in ref. [85]. While higher sensitivity to changes in bulk refractive index can be achieved using SPR spectroscopy, LSPR is useful for interrogation of short-range changes associated with adsorbate layer. Overall, the responses are typically comparable. SPR sensitivities are strongly dependent on the prism material, excitation wavelength and dielectric constant of the metal film. The typical reported SPR sensitivity lies in the range 100–300° RIU^{−1} or 5500–7500 nm RIU^{−1} for gold metal film based sensors [85,86]. Selected examples of LSPR sensitivities for a range of nanostructures are presented in Table 1.

Flexibility in the selection of LSPR substrate allows tuning of wavelength throughout the visible spectrum, the near IR and into

Table 1
LSPR sensitivities for nanostructures used for wavelength shift based detection.

Nanostructure	Size (nm)	λ_{LSPR} (nm)	Sensitivity (nm RIU ^{−1})	FOM (RIU ^{−1})	Reference
Au nanospheres	13, 15, 30, 50	520	76, 44, 71, 60	0.6	[100,193,194]
Au nanoshells hollow	50 (wall 4.5 nm)	680	409	NA ^{−1}	[100]
Au nanoshells/SiO ₂ core	50–175	Varies	570–996	NA ^{−1}	[195]
Au nanorings	75–150	1058–1545	880	NA ^{−1}	[40]
Au nanorods	74 (<i>d</i> = 33) 40–74 (<i>d</i> = 17)	700 653–846	252 195–288	1.7–2.6	[95,194]
Au nanorice/hematite core	9.8–27.5 ^a	1160	800	NA ^{−1}	[88]
Au nanocubes	44	538	83	1.5	[194]
Au nanobipyramids	27–189	645–1096	150–540	1.7–4.5	[194]
Au nanostars	100	647, 700, 783	879 ^c	10.7	[196]
Au metamaterial	400 × 80 and 340 × 90 ^b		588	3.8	[197]
Ag nanosphere	40–90	400–480	160	NA ^{−1}	[198]
Ag nanoprism	55–120	600–700	200–350	2.3–3.3	[198,199]
Ag nanoprism/Au coated	21–22	940	470	NA ^{−1}	[82]
Ag array (NSL)	Varies	500–700	200	NA ^{−1}	[200]
Ag nanocubes	30	430	1569 ^d	5.4	[87]

^a Shell thickness.

^b H-shaped cut-out structure in 30 nm gold film.

^c Value converted to nm RIU^{−1} from 1.41 eV RIU^{−1}.

^d Value converted to nm RIU^{−1} from 0.79 eV RIU^{−1}.

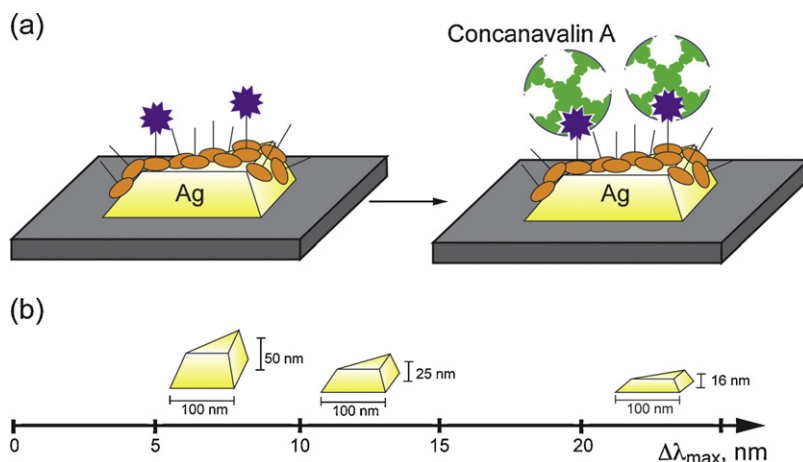


Fig. 5. (a) Real time response of concanavaline A binding to mannose functionalized Ag NPs of different height. (b) Schematic of experimental setup used in concanavaline A Ag nanobiosensor. Adapted with permission from Reference [101]. Copyright 2004 American Chemical Society.

the IR. Selection of geometrical structures of higher complexity provides for greater sensitivity in comparison to spherical NPs. The LSPR sensitivity is described by its figure of merit (FOM) and defined as the ratio of wavelength shift per refractive index unit change divided by the full-width-at-half-maxima (FWHM) of the LSPR peak [87]. Although this approach accounts for the position and width of LSPR peak, most studies report absolute shifts. The magnitude of wavelength shift is LSPR resonance position dependent exhibiting an increase with redshift of LSPR [82,88]. To date, researchers have designed LSPR assays based on NPs immobilized on surfaces, assembled into periodic particle arrays and as nanohole arrays. Structured arrays and nanoclusters exhibit Fano resonances as a result of interference between coupled plasmon modes and can offer high sensitivity to the dielectric environment [89–91].

Some early efforts made use of gold and silver nanospheres, using biotin–streptavidin interaction for immobilization of biomolecules. Optimization of the size of NPs allowed achievement of a limit of detection (LOD) for streptavidin of 0.83 nM [92]. In assays that probed antigen–antibody recognition events with human or bovine serum albumin, the LOD achieved was 10 nM [93]. Quantitative detection of smaller molecules such as the steroidal hormone stanozol was also done using a similar approach, and the LOD of 2.4 nM was much lower than the minimum required performance level (MRPL) set by the International Olympic Committee (IOC) for banned substances [94].

Nanorods offer a greater sensitivity to bulk refractive index changes than that achieved from nanospheres. The longitudinal LSPR for a nanorod with aspect ratio of 3 was shown to have six times higher sensitivity [15]. The biosensing capability investigated with streptavidin–biotin interaction provided a LOD of 94 pM in buffer solution and 19 nM for serum samples using Au nanorods with an aspect ratio of 2.2 [95]. The dynamic range for this assay spanned almost six orders of magnitude from 94 pM to 0.19 μ M. The same group later attempted streptavidin detection on single nanorods using dark-field microscopy by tracking the wavelength shift in real time. The detection for a concentration of 1 nM streptavidin was achieved with reproducible mean wavelength shift of 0.59 nm for this assay [96].

Bioassays for detection of pathogenic bacteria, *Escherichia coli* and *Salmonella typhimurium*, were reported by Wang and Irudayaraj using amine-modified Au nanorods that had been coated with covalently coupled antibodies [97]. Selection of two types of nanorods with different aspect ratio (2.0 and 3.2) and thus different longitudinal LSPR peaks allowed for the simultaneous monitoring of two different species of pathogens [97]. Yu and Irudayaraj

have shown a multiplexed assay based on gold nanorods interrogating binding events with three targets of immunoglobulin G: goat-antihuman IgG1 Fab, rabbit anti-mouse IgG1 Fab, and rabbit anti-sheep IgG (H+L) [98]. Gold nanorods with aspect ratio varying from 2.3 to 6.5 were activated with a self-assembled monolayer (SAM) of mercaptoundecanoic acids (MUA) on the {111} facets while retaining CTAB capping at {110} and {100} facets. Formation of carboxylic acid functional groups on the surface facilitated the covalent coupling of antibodies through amide bonds. The transverse LSPR was sensitive to refractive index changes upon binding of IgG with a typical wavelength shift of only about 3 nm, while longitudinal LSPR, depending on aspect ratio, exhibited redshifts from 11 to 27.5 nm.

Metal nanoshells exhibit increased refractive index sensitivity with decrease in shell thickness. For a silica core–gold shell NP, Jain et al. found a near-exponential decay in sensitivity with an increase in the ratio of nanoshell thickness to core radius [99]. This scaling behaviour was explained in terms of the ease of polarization of electrons by light due to EM coupling of the inner surface cavity plasmon and outer surface sphere plasmon. An even more intriguing phenomenon with respect to bioassay and biosensing applications was observed with hollow nanoshells. Sun and Xia found that hollow Au nanoshells with thickness of ca. 4.5 nm and a NP radius 25 nm were over six times more sensitive to solvent and SAM modifications in comparison to Au nanospheres of the same size [100].

Numerous bioassays and sensing constructs have been reported using structured nanoarrays fabricated by NSL or NIL. The primary advantage of this approach is elimination of the issue of aggregation of NPs, which is usually accomplished by introducing capping ligands to control colloidal stability. Early investigations of nanoarrays reported use of the well established biotin–streptavidin model. For example, a triangular array of Ag nanoparticles provided a LOD of 0.7 nM, which was comparable to previously described nanostructures that were dispersed in solution. A biosensor based on Ag triangular NPs array was used to monitor the real time binding of concanavalin A to NPs that were surface functionalized by addition of the monosaccharide mannose (Fig. 5b) [101]. The conjugation chemistry began with triethylene glycol disulfide and maleimide disulfide incubation for 12 h. The resultant maleimide terminated moiety on the surface of NPs was coupled to mannose-thiol, forming a stable disulfide bond. The LSPR peak of the mannose functionalized Ag nanosensor at 636.5 nm was observed to and incubation in ca. 20 μ M concanavalin A, followed by rinsing in buffer resulted in 17.8 nm redshift. The magnitude of redshift upon

binding was investigated by varying the out-of-plane height of the Ag NPs (16, 25 and 50 nm) as shown in Fig. 5a [101]. The strongest LSPR shift was observed for thinner NPs, which agree with the distance dependent studies, while as anticipated the kinetic rates of binding process were independent of the geometrical configuration.

An example of potential for biomedical screening is based on use of Ag triangular arrays for detection of Alzheimer's disease biomarker using two different approaches. For one method, amyloid-beta-derived-diffusile (ADDL) ligand antigen was immobilized on the surface of NPs coated with SAM of MUA and 1-octanethiol [102]. ADDL antigen coupling was achieved using 1-ethyl-3-(3-methyl-aminopropyl)carbodiimide hydrochloride (EDC) for the formation of an amide bond. Finally, the binding of specific rabbit polyclonal anti-ADDL IgG antibody was studied, and the associated saturation of LSPR response provided a 18.5 nm shift at a concentration of 100 nM of anti-ADDL. The challenge encountered in the course of these experiments was a strong non-specific adsorption of anti-ADDL at lower concentration to the chromium adhesion layer, which is commonly used in nanobiosensor fabrication [102].

A second method made use of a sandwich immunoassay format [103]. In order to eliminate non-specific adsorption associated with the Cr layer, the glass slide was substituted with mica allowing for direct adhesion of NPs to the surface. The surface that was coated with NPs was modified with ADDL antigen, then incubated with anti-ADDL antibody, and finally a sandwich assay was done by introducing another capping layer of ADDL antigen. The associated LSPR shifts with each step were 4.2 nm, 7.6 nm and 1.9 nm, respectively. An additional 3.4 nm shift was observed for a further incubation with antibody, giving rise to a total LSPR shift of 5.3 nm as an analytical signal [103]. This method was applied to clinical samples of human brain extracts and cerebrospinal fluids (CSF) from Alzheimer's patients. For the CSF samples, a shift of 28.5 nm was observed upon binding of ADDL and a further shift of 15.4 nm occurred on addition of capping antibody. The brain extract resulted in a more modest total shift of 10.7 nm.

Significant improvement of an LSPR bioassay with 400% amplification of shift upon antibody binding to analyte was demonstrated using antibodies that were labeled with gold NPs [104]. Biotin specific IgG antibodies were labeled with 20 nm gold NPs and introduced to a biotin functionalized silver nanoprism array. The induced wavelength shift was 42.7 nm, while unlabeled anti-biotin resulted in only a modest 11 nm redshift. The authors also noted improvement in the binding constant by two orders of magnitude for antibody–NP conjugate.

An optical fiber tip modified with Au nanodot arrays generated by e-beam lithography offers another approach in biochemical sensing. The advantages of this system include robustness of mechanical design and potential for reusability. Based on the biotin–streptavidin model, the detection limit of 6 pM was reported, with a corresponding wavelength shift is 5.4 nm, and a sensitivity of 196 nm per RIU was demonstrated for the optical fiber LSPR sensor design [105].

The LSPR wavelength shift depends on the optical mass of the analyte as shown by Eq. (8). Therefore, the most common targets are typically larger proteins that induce significant wavelength shift and are easily transduced. However, Zhao et al. designed a smart biosensor based on binding of low molecular weight substrate to cytochrome P450. By taking advantage of an intrinsic chromophore within the biomolecule and using LSPR of slightly longer wavelength than the adsorbate's molecular resonance wavelength, the spectral shifts were found to increase by a factor of three. The NSL fabricated Au NPs were coated with a SAM of MUA and 1-octanethiol. The conjugation of cytochrome P450 cam protein (CYP101)(Fe³⁺) was done with EDC coupling through amide bond

formation with free carboxylic groups on the MUA layer. The red shift for the conjugation process was found to be 13.2 nm. Subsequent exposure of the substrate to the target camphor blue resulted in an LSPR shift of 8.7 nm [106]. This example illustrates potential of detecting small molecules by selection of LSPR to be close to electronic resonance in order to induce detectable LSPR shifts.

Another nanostructure array used for biosensor design is the nanohole array. This structure combines the properties of surface plasmon resonance associated with thin metal films and LSPR. Although, designs based on disordered nanohole assemblies prepared by NSL or colloidal lithography have been reported, the focus of the following section is dedicated to systems that use ordered arrays. Ordered structures are usually prepared by focused ion milling (FIB) and soft embossing techniques. A biotin–streptavidin binding interaction was monitored with a nanohole biosensor and yielded a 10 nm LSPR shift for a 30 × 30 array [107]. Assuming full coverage of each hole with streptavidin, and a size for streptavidin of 25 nm², ca. 2000 molecules were probed in each hole, which corresponds to 3 attomoles of protein [107]. In another example, a nanohole array that was modified with a cortisol derivative was used for binding of monoclonal antibody. Enhancement of signal was achieved by introducing a construct based on a secondary antibody coupled with a Au NP. The immunochemical binding of monoclonal antibody to cortisol, resulted in a 2 nm shift, while a NP enhancement gained by introducing secondary labeled antibody resulted in a 7 nm LSPR shift [108].

Multiplexed sensing for rapid, label-free detection of antigen–antibody binding was developed in a multichip nanochip with 300 sensing spots separated by 1 mm [109]. This biochip provided detection of protein concentrations in nanoliter volumes. The fabrication consisted of coating a glass slide with a thin film of gold, then placement of silica beads onto this surface, followed by the deposition of another layer of gold. The core-shell array of NPs was functionalized with a SAM of (4,4'-dithiobutyric acid). Next, six different antibodies were immobilized: anti-IgA, anti-IgD, anti-IgG, anti-IgM, anti-CRP and anti-fibrinogen in concentrations ranging from 1 fg mL⁻¹ to 1 mg mL⁻¹. Introduction of the corresponding target resulted in a change in absorbance for various concentrations. The LSPR spectra were acquired with a fiber-coupled UV–vis spectrometer using a reflective geometry. The LOD for this biochip was 100 pg mL⁻¹ and linear response extended up to 1 µg mL⁻¹.

An advantage of LSPR is associated with its potential for miniaturization, where the conventional SPR Kretschmann configuration poses some limitations. Prisms used in total internal reflection mode create complexity for assembly of miniaturized lab-on-a-chip detectors. An LSPR biochip designed by Hiep and coworkers was fabricated using NSL to place gold NPs on the surface [110]. Real-time detection of insulin using an antigen–antibody reaction was done, and provided an estimated limit of detection 100 ng mL⁻¹ insulin and a linear range from 0.1 to 10 µg mL⁻¹. In a separate study, 43 nm citrate capped colloidal gold NPs were immobilized on a quartz substrate and further integrated into microfluidic device [111]. Specific amounts of bio-samples were transported into sensing chambers, and high sensitivity and specificity with rapid reaction times and minimal reagent consumption was noted. As a proof-of-concept, the authors detected biotin/anti-biotin binding and measured the sensitivity of a device (62 nm RIU⁻¹) using glycerol solution.

5.1.1. Nanoplasmonic molecular rulers and PRET biosensors

Nanoplasmonic molecular rulers (PMRs) allow for label-free measurements of DNA and protein length/size and distance changes, real-time kinetic measurement of protein–ligand and nucleic acid interactions, and determination of the presence of enzyme activity. PMR offers significant advantage in comparison to the popular method of Förster Resonance Energy Transfer (FRET)

for long-term kinetic studies, as conductive NPs do not photobleach or blink. Furthermore, in comparison to FRET, which interrogates binding and conformational events over a 1–10 nm range, PMR offers transduction of binding events with separation distances of up to 70 nm.

Dimers of Ag or Au NPs have been used for DNA length measurements and tracking of hybridization kinetics. The distance between two NPs was determined on the basis of plasmonic coupling [10]. Single stranded DNA (ssDNA) with a terminal thiol and also biotin functionalization was conjugated to Au NP by self-assembly of the thiol moiety. Streptavidin coated Au NPs were then introduced, and the distance between NPs was set by the ssDNA and modulated by changing of the ionic strength of the buffer. High (0.1 M NaCl) salt concentration resulted in charge screening along the backbone of ssDNA, allowing closer approach of the NPs with a resulting red shift in LSPR. At lower salt concentration (0.005 M NaCl), increased electrostatic repulsions led to a blue shift of the LSPR. Hybridization of complementary DNA increased the separation between two NPs because dsDNA has more rigid structure. This resulted in significant blueshift of the LSPR maximum (Fig. 6a). Recording of the time dependence of spectral shifts allowed elucidation of kinetics

of hybridization, and observation of a multi-step process of attachment/detachment associated with inefficient hybridization of oligonucleotides immobilized on the surface of NPs [10].

A correlation between LSPR shift and inter-particle separation is achieved with a scaling model (Eq. (12)). The model was shown to be in good agreement with experimental data [112].

$$\frac{\Delta\lambda}{\lambda_0} = 0.18e^{-s/0.23D} \quad (12)$$

A further investigation focused on study of nuclease activity, and observed the wavelength shift due to the changes in dielectric constant upon changes in DNA length as a function of time. An average shift of 1.24 nm per base pair was observed [113].

Plasmonic resonance energy transferred from NPs to biomolecules in close proximity serves as label-free transduction method that offers 100–1000 times more sensitivity in comparison to organic molecular dyes that are used as reporters. Overlap of NP spectra with the absorption spectra of biomolecules promotes PRET, resulting in wavelength dependent quenching of Rayleigh scattering as is illustrated by Fig. 6b [7,114]. Plasmonic quenching of Au NPs with cytochrome c was used to monitor

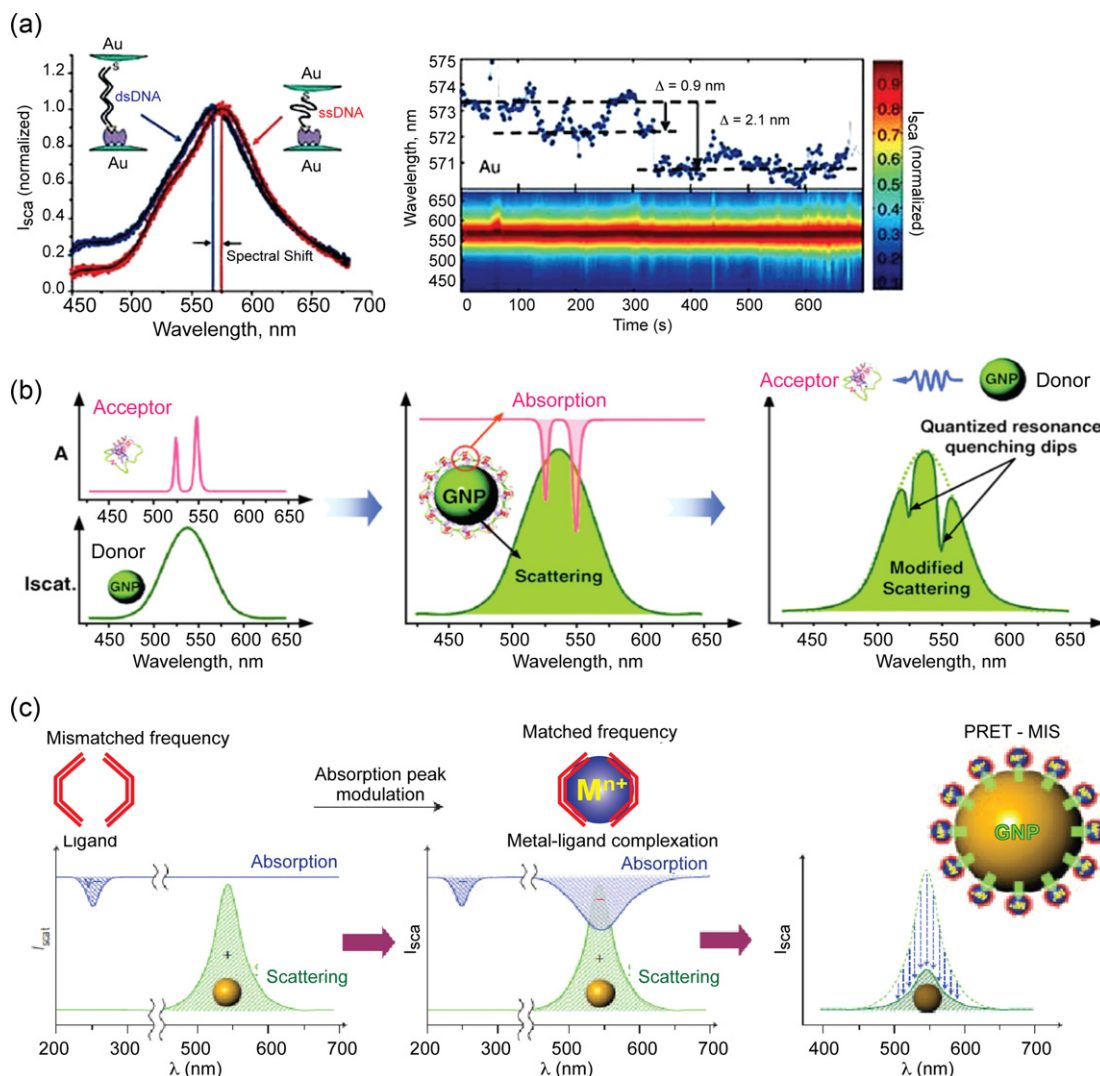


Fig. 6. (a) Nanoplasmonic molecular ruler for detection of DNA hybridization with Au NP dimer. Spectral shifts observed real time upon changes in ionic strength due to the changes in NPs separation distance. Adapted by permission from Macmillan Publishers Ltd: Nature Biotechnology [10], 2005. (b) Mechanism of PRET, where plasmon resonance energy is transferred from NP to cytochrome c. Left: typical spectrum of Au NP and cytochrome c in bulk; centre: spectral overlap of Rayleigh scattering of NP and absorption spectrum of biomolecule; right: quenching in Rayleigh scattering spectra due to PRET. Adapted with permission from Reference [7]. Copyright 2009 American Chemical Society. (c) Left: no spectral overlap between ligands and NPs; centre: absorption spectrum of metal–ligand complex matches the Rayleigh scattering spectrum; right: quenching of Rayleigh scattering. Adapted by permission from Macmillan Publishers Ltd: Nature Nanotechnology [8], 2009.

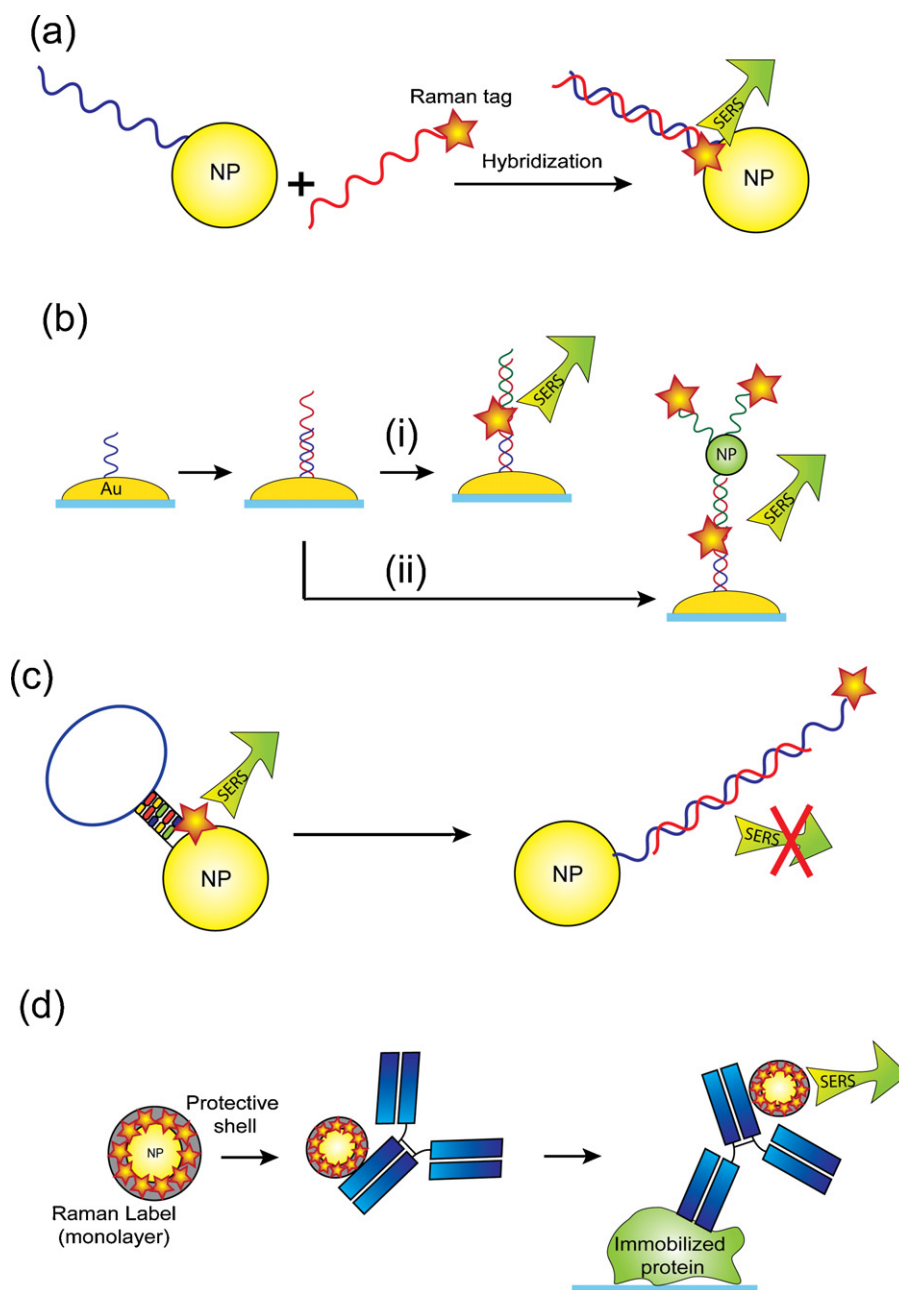


Fig. 7. SERS based detection designs. (a) DNA hybridization detection with Raman tag labeled complementary target oligonucleotide. (b) NP array substrate used in sandwich assay, (i) direct detection with Raman tag labeled reported and (ii) enhanced sensitivity achieved by introduction of secondary NP conjugated to reporter oligonucleotide. (c) Molecular beacon design used to detect a reduction in SERS signal. (d) Schematic illustration of immunodetection using Raman label encapsulated in protective layer (e.g. silica shell) and functionalized with antibody for enhanced selectivity.

real-time production of protein in HepG2 cells using dark-field microscopy. The same group developed a sensitive and selective PRET-based sensor for Cu^{2+} ion [8]. The d-orbitals of the transition metal splits upon formation of metal–ligand complexes generating different absorption bands. Quenching results when the Rayleigh scattering frequency is matched with the absorption band of the metal–ligand complexes (Fig. 6c).

5.2. SERS-based bioassays and biosensing

Applications of SERS with NPs can be classified into two distinct groups: label-free detection, and approaches that use SERS labels for the identification of biomolecules. The former technique is widely used to obtain SERS spectra of an analyte that is

adsorbed to the surface of a NP, while the latter uses NPs that are overcoated with molecules that exhibit a characteristic Raman vibrational mode and that are used for the indirect identification of biomolecules.

SERS detection can be achieved either in a solution phase (homogeneous assay) where analyte interacts with free NP, or at a solid phase interface (heterogeneous assay) where a substrate that is activated with NPs is used to probe target binding. The solution phase assay offers reproducibility and high kinetic rates, but typically suffers from low detection sensitivity due to a high degree of dispersion within the sensing volume. SERS-active substrates have been developed using roughened metal electrodes (several oxidation–reduction cycles), metal island films, and surface assembly. Despite numerous advantages of solid phase assays, the major

challenge remains the consistent production of reproducible substrates that define the EF. Reliable detection requires an ability to control interparticle separation to achieve reproducible hot spots and field amplifications. In addition, it is necessary to place analyte into interparticle junctions to achieve maximum enhancement. An elegant approach to control structure was demonstrated recently by Taylor and coworkers [29]. Cucurbit[*n*]uril (CB[*n*]) is a barrel-shaped molecule comprised of *n* (5 or 7) glycoluril units. A polar carbonyl exterior can bind to the surface of Au NPs, and a hydrophobic interior can capture an analyte molecule. CB[5] placed Au NPs precisely 0.9 nm apart through induced aggregation to create an intense confined electric field. Additionally, CB[*n*] is Raman active and can serve as self-calibrated SERS substrate.

Some examples of SERS biosensors for label-free detection have appeared, such as for determination of glucose [115,116], lactate [117], dipicolinic acid – an anthrax biomarker [118], calcium dipicolinate (CaDPA) [119], and gaseous 2-chloroethyl ethyl sulfide (CEES) [120] – a compound related to detection of mustard gas. These designs used Ag FON substrates that were either bare or alumina-modified to provide an increased stability and enhanced binding affinity of the substrate. A portable sensor for detection of aniline and phenol derivatives using on-site electrostatic pre-concentration has been reported by Long and coworkers [121]. Silver electrodeposited screen-printed electrodes served as SERS substrates, while applying different potential allowed selective adsorption of polar organic pollutants. Under optimum conditions quantification was possible over the range 1 nM to 1 μ M.

The applicability of SERS technology for *in vivo* applications was illustrated by Stuart et al. with introduction of a glucose sensor [122]. Silver FON substrate was modified with a SAM of decanethiol and mercaptohexanol that allowed for reversible adsorption of glucose. In an unrelated study, evaluation was done of the potential of *in vivo* detection of squamous dysplasia – a precursor to cervical cancer [123]. Raman spectra were collected directly from the cervical epithelium using 789 nm excitation. The authors found that the signal intensities of bands at 1330, 1454 and 1656 cm^{-1} could be used to distinguish high-grade squamous dysplasia.

5.2.1. Nucleic acid hybridization assays

Bioassay and biosensing techniques have been developed using NPs for detection of DNA hybridization, protein interactions, and identification of intracellular molecular events. Huh et al. detected DNA hybridization in a microfluidic device using 50 nm Au NPs that were functionalized with thiol-terminated ssDNA [124]. The NPs were passivated with 6-mercapto-1-hexanol to reduce non-specific adsorption. Target nucleic acids that were modified with tetramethylrhodamine (TAMRA), and hybridization brought the dye into close proximity to the surface of the NP (Fig. 7a). The presence and intensities of Raman signals characteristic of TAMRA in SERS spectra were used to transduce hybridization. Recently, a sandwich assay for DNA hybridization using SERS was reported. A layer of capture ssDNA containing thiols was immobilized on the surface of Ag nanoislands, followed by introduction of target oligonucleotide was (Fig. 7b). The authors investigated two methods: probe labeled with a Raman tag, and Au NP capped with probe that was labeled with a Raman tag. The introduction of NPs for implementation of the sandwich assay format resulted in enhancement of target detection from 1 nM to 0.4 fM [125]. The choice of organic dye is governed by its SERS activity and compatibility with DNA hybridization. The intensity of the SERS signal needs to be strong and unchanged during hybridization, and unlabelled DNA should not exhibit SERS signal interferes with the signal from the dye.

Molecular beacons have also been investigated, where the DNA hairpin structure is modified with a Raman active molecule and is attached to a NP [126–128]. The process of hybridization with

complementary target disrupts the loop configuration, increasing the distance of the Raman active molecule and thus reducing the SERS signal (Fig. 7c). The distance dependence of LSPR in this case between a NP and the Raman label is the basis of the detection scheme.

5.2.2. Protein detection assays

Protein detection and analysis is commonly achieved using NP aggregates, nanostructured surfaces and Raman labels. The group of Moskovits studied small FynSH3 proteins, which upon reduction have two cysteine moieties at axially opposite sites, acting as bifunctional ligands [129]. In the presence of Ag NPs, they induced the assembly of dimers and aggregates, which in turn provided enhancement for SERS. Due to the intrinsically small size of the protein (2.3 nm) the junction points act as “hot spots”. However, since the “hot spot” effect is highly localized and drops off significantly as shown in Fig. 1, no tryptophan or phenylalanine peaks were observed. This study illustrated the significance of protein orientation with respect to the “hot spot” region. Aggregate formation was also exploited by the group of Stevens for the detection of disease-specific enzyme [130]. Au NPs (ca. 40 nm) were functionalized with *N*-(fluorenyl-9-methoxycarbonyl) (FMOC) terminated peptide. The aggregation was driven by π - π interactions between FMOC groups, and these could also serve as reporters using SERS. The addition of thermolysin enzyme resulted in the promotion of de-aggregation, and a corresponding decrease in Raman response was noted. The potential detection limit of this system was estimated as 10^{-13} M, while experimental data obtained a LOD of 10^{-11} M, which is still an order of magnitude lower than what is required in medical applications.

Au NPs functionalized with thrombin were detected on antithrombin III and heparin modified glass slides [131]. The Raman marker used was a diazo bond that linked thrombin to NPs. A LOD of 10^{-13} M was determined for thrombin based on SN^{-1} ratio of 3. Li et al. have illustrated detection of IgG using Au NPs functionalized with protein A, while fluorescein coupled to NPs using avidin-biotin interaction served as Raman labels [132]. A LOD of 1 ng mL^{-1} with dynamic range over three orders of magnitude was reported. Detection capabilities that surpass any reported for organic dye Raman labels have been noted when single-walled carbon nanotubes (SWNTs) are implemented [133]. Due to an enormous Raman scattering cross-section of ca. $10^{-21} \text{ cm}^2 \text{ sr}^{-1} \text{ molecule}^{-1}$ for SWNTs, femtomolar protein concentrations were detected on a random array of metal nanoclusters. The immobilization of protein was done on PEGylated surfaces to minimize the background from non-specific adsorption, and SWNTs were tagged with antibody. “Two color” multiplexing was achieved by use of isotopic ^{12}C and ^{13}C SWNTs. The authors reported detection at clinically relevant concentrations of a granulomatosis biomarker for an autoimmune disease (aPR3) in native serum.

5.2.3. SERS Raman labels

Plasmonic NPs enhance Raman signatures of a molecule when they are in close proximity to each other. Efficiency of a SERS signal is enhanced even further for Raman reporter that is adsorbed directly to the surface of NP. Nitrogen and sulfur containing molecules are often used due to the great affinity to metals such as silver and gold. Raman reporter molecules are often aromatic molecules with intrinsically strong Raman scattering, and are coated on NPs in monolayer or sub-monolayer coverage. In order to increase sensitivity a large number of reporters (10^3 – 10^4) can be coated on each NP [134]. Schlucker and coworkers have shown a complete SAM yields almost 22 times more intense SERS signals in comparison to sub-monolayer coverage [135]. Encapsulation of SERS labels with silica shell [136–138], organic polymers [139]

and proteins [140] improves the stability, eliminates the possibility of desorption of Raman reporters and minimizes the non specific adsorption. Coating with silica creates a robust structure and provides long-term stability. Such constructs have been commercialized by Oxonica as Nanoplex biotags. Encapsulated SERS aggregates or assemblies, despite larger sizes provide a tremendous enhancement in SERS intensities [141]. SERS labels conjugated with antibodies provide selectivity and specificity of detection and have been used in SERS-based immunoassays [142,143]. A schematic representation of immunohistochemical assay using a SERS label is shown in Fig. 7d. Multiplexing was achieved with SERS labels by using a range of dyes, and the method was used for DNA detection [141,142,144], and investigation of protein–small molecule interactions [142].

5.2.4. Intracellular detection

Living eukaryotic cells are complex entities that undergo a multitude of dynamic processes giving rise to cell function. Nanoplasmonic particles have been used for cell imaging, to probe drug–cell interaction, and photothermal therapy. A variety of nanostructures including Au nanospheres, nanorods, and nanoshells that exhibit strongly enhanced absorption in the visible and near-infrared region (NIR) have been used as thermal converters to instigate irreversible damage of cancerous cells [145].

Intracellular assays and biosensing based on LSPR is still in its infancy; however, such methods have potential for applications in biomedical diagnostics, drug delivery and determinations of therapeutic efficacy at the cellular level. Drug uptake on plasma membrane of living cells was monitored with high sensitivity (10^{-10} M) by SERS for antitumor drug mitoxantrone (MTX) [146]. Kniepp et al. investigated drug diffusion through cell membrane using Au and Ag NPs and nanoaggregates that were delivered intracellularly by endocytosis [31,147]. NPs are typically incubated with cells in culture medium for several hours leading to endocytosis and sequential ingestion. Diffusion of anticancer drug emodin through membrane of U87-MG cancer cells was studied using silver coated silica beads, and the data demonstrated the capability of observation of the kinetics of diffusion [148]. Shamsaie et al. reported intracellularly grown Au NPs (IGAUNPs) within MCF10 epithelial cells. Unlike Au and Ag NPs, IGAUNOs were not translocated to the endosomes and lysosomes, which was confirmed by the absence of Raman bands around 500 cm^{-1} associated with stretching vibrational mode of disulfide bonds that are abundant in lysosomal proteins [149]. An approach to deliver SERS probes to the cell nucleus was demonstrated by co-functionalizing NPs with HIV-derived “Trans-Activator of Transcription” (TAT) peptide along with Raman reporter molecule [150]. Electroporation allowed for rapid uptake of NPs by the cells, and the Ag NPs in the cell cytoplasm became highly localized [151].

Detection of breast cancer cells in blood samples was achieved using a combination of magnetic nanoparticles that were overcoated with epithelial specific antibody (EpCAM) and anti-her2 antibody conjugated to Au NPs that could provide SERS [152]. The modified magnetic beads specifically bound to the epithelial cells, while anti-her2-SERS tags recognized cancer cells with over-expressed her2 receptor. The LOD was less than 10 cells mL^{-1} , and negative control experiments indicated negligible nonspecific binding of the SERS tags to the magnetic beads. This method provided high specificity and good sensitivity using whole blood samples. Au NPs modified with polyethylene glycols (PEGs) and encapsulated Raman reporters were used by Nie and coworkers for *in vivo* targeting of tumors [153]. The PEG coating provided enhanced colloidal stability of Au NPs over wide range of pH and ionic strength. However, the coating presented a compromise in that it increased the hydrodynamic diameter by 20 nm. These nanotags were covalently conjugated to an ScFv antibody that bound

with high specificity and affinity to EGF receptor on tumor cell surfaces.

5.3. Metal enhanced fluorescence (MEF)

Nanoparticles have historically been used in luminescence quenching, and it is only over the last decade that in-depth studies of MEF began to appear. In previous sections it has already been indicated how the choice of nanostructure can impact detection based on LSPR. Selection of the substrate for MEF is even more crucial in achieving high enhancement factors. Consider the following parameters that influence MEF:

- (i) Larger NPs induce stronger MEF (60–80 nm diameter).
- (ii) Anisotropic NPs are more effective in comparison to isotropic (e.g. spherical).
- (iii) Spectral overlap of NP plasmon resonance with excitation and/or emission spectra of fluorophore alters field strength.
- (iv) NP–fluorophore separation distance represents a compromise between competing processes associated with enhancement and quenching.
- (v) Excitation wavelength dependence can alter the radiative and non-radiative decay rates.
- (vi) There can be angular dependence.

Given these considerations, there are a number of challenges in the engineering of an MEF substrate to achieve maximum enhancement efficiency. As a result, each case typically requires tuning and optimization of experimental conditions. Reported enhancement factors range from two to a few hundred, and NPs can efficiently scatter light with angular dependence resulting in increased fluorescence emission [154].

A variety of observations follow that indicate the complexities that are confronted when considering design criteria. Scattering efficiency of NPs is size dependent. Silver NPs of 30 nm size scatter light nine times more efficiently than Au NPs of the same size at 530 nm, and 124 times more than polystyrene NPs [5]. Silver NPs smaller than 30 nm mainly exhibit absorption, but scattering dominates the extinction spectrum in NPs larger than 50 nm [155]. Multiple LSPR peaks of anisotropic NPs increase the probability of coupling of excited state fluorophores to LSPR modes. Strong electric fields present around NPs, and even stronger fields between NPs, promote effective absorption of light by a chromophore. The intensity of electric field is greater at resonance, indicating that a maximum interaction between NP and chromophore occurs when there is spectral overlap [156,157]. Theoretical and experimental studies have shown that maximum fluorescence enhancement is observed when the emission maximum of fluorophore is slightly red shifted with respect to an LSPR scattering peak [157,158]. At the resonance condition the radiative and non-radiative decay rates are enhanced. A blue shift of an LSPR peak correlates with greater decrease of non-radiative decay rates in comparison to radiative decay rates. This in turn leads to the overall fluorescence enhancement.

Quantum dots have been used due to their large Stokes shifts to investigate contributions from excitation enhancement and emission enhancement. The emission enhancement was noted to be strongly wavelength dependent, and a maximum enhancement factor was observed when an LSPR peak overlapped with photoluminescence (PL) spectra of QDs [156]. The excitation enhancement was dependent on the excitation wavelength, and was maximized when the wavelength of excitation coincided with an LSPR scattering peak [159]. The excitation enhancement factors ranged from 10 for Ag nanoprisms to 3 for Au spheres (80 and 100 nm) and Ag nanocubes (50 nm). The quantum yield and PL lifetime of quan-

tum dots were strongly influenced by excitation wavelength in the presence of silver nanoparticles [160].

The distance dependence of fluorophore–NP was discussed previously, and has typically been evaluated experimentally using Langmuir–Blodgett (LB) monolayers or Layer-by-Layer (LBL) film assembly [161,162]. At shorter distances (0–5 nm) fluorophore quenching is observed. At longer distances up to about 15 nm there is variation of the excitation field, and at distances up to 20 nm there is modification of the radiative decay rate of fluorophores [163].

Even though an MEF assay method has many variables, it does offer increased photostability of fluorophore, decreased lifetime, increased quantum yield, and distances between donor and acceptor that are suitable for FRET [164]. Self-quenching of fluorophore by neighboring fluorophores (fluorescein, cyanine dyes) can also be eliminated in the presence of metal NPs [165–168].

MEF transduction has been applied to detect DNA, RNA, proteins and metal ions. These assays were based on silver island films [169–173], colloidal NPs [174–176], Ag nanoprisms [157], nanotriangles [177], nanorods [178] and structured arrays [179]. Silver island films (SiFs) can support multiple surface plasmons as a result of complex geometrical structure and have served as substrates of choice in numerous studies. Thermally annealed colloidal substrates produce higher fluorescence enhancement [180]. SiFs increased by two- to three-fold the fluorescence emission from Cy3 and Cy5 labeled DNA [181]. An increased sensitivity of a DNA microarray was achieved by immobilizing a biotinylated 23 base pair probe on SiFs that were functionalized with avidin [182]. Complementary targets contained either Cy3 or Cy5. The extinction maximum of bare SiF was at 420 nm and redshifted to 500 nm for avidin–SiF as a result of change of refractive index. The maximum fluorescence enhancement was ca. 10-fold for Cy5 and 3-fold for Cy3 with redshifted absorption and emission relative to LSPR peak. Higher enhancement factors (28-fold and 4-fold for Cy5 and Cy3) were observed with pre-hybridization in solution followed by spotting on avidin–SiFs. These differences were attributed to the respective efficiencies of surface hybridization. Maximum fluorescence intensities were observed between 6.25 and 12.5 μ M and decreased at higher concentrations primarily due to decreased hybridization efficiency.

The kinetics of surface hybridization can be significantly improved, going from hours to seconds, by using low power microwave heating in MEF assays. This method first described by Geddes and coworkers was termed microwave-accelerated metal enhanced fluorescence (MAMEF). The water and glass associated with the reaction vessel become heated under microwave radiation, while metal NPs remain at the same temperature thereby creating a temperature gradient. This leads to a rapid transfer of molecules (e.g. proteins, oligonucleotides) from warmer bulk solution to the colder surface of NPs [183]. A proof-of-concept application was demonstrated using biotin–avidin interaction [184,185]. Fluorescence emission of fluorescein isothiocyanate (FITC) was amplified 10-fold while assay times accelerated by microwave radiation were 90 times faster in comparison to room temperature control assays. MAMEF-based DNA hybridization assays were kinetically complete in 20 s accelerating hybridization kinetics by 60-fold [186]. Thiol modified oligonucleotide probes were self-assembled on SiFs followed by hybridization with complementary fluorescein-labeled target using a concentration range 50–1250 nM. The stability of oligonucleotide probe to low power microwave heating was confirmed by melting and re-hybridization. This platform was used in 1-color assay for detection of DNA from *Bacillus anthracis* spores and vegetative cells [187]. The DNA was efficiently released from spores using microwave bursts in combination with aluminium triangles assembled in a bow-tie configuration. The 12.5 mm gaps between triangles focused the

microwave energy and resulted in significant temperature jumps and cellular disruption. The MAMEF on SiFs detected DNA extracts from 100 organisms mL^{−1} in less than 30 s. The same research group recently presented a two-color DNA detection scheme based on MAMEF [188]. Two different oligonucleotide targets were labeled using Alexa 488 and Alexa 594 for this work.

Analysis of whole blood samples using MAMEF was shown by Aslan using biotin functionalized BSA (b-BSA) [189] and Troponin I [172]. The detection of less than 0.01 nM b-BSA was achieved with a total assay time of 1 min, while LOD of Troponin I was 0.05 μ g L^{−1}. Detection of the chromosomal *oriC* DNA sequence from lysed *Salmonella* with TAMRA labeled reporter has been reported. As little as 1 colony forming unit (CFU) of *Salmonella* in 1 mL of medium was detected in under 30 s [190]. The viscosity of blood was suspected to impede the mass transport in MAMEF assay and dilution in 1:1 ratio with buffer enabled the detection [190].

6. Prospective and conclusions

This review has highlighted the theory and applications of LSPR for detection of biomolecules. A survey of transduction techniques and substrate engineering approaches has been presented to indicate the potential and the challenges for improvement of the sensitivity of detection. An appreciation of fundamentals of LSPR offers opportunities to tune and control optical behaviour. A strong dependence of LSPR on NP shape, size and composition provides a means to improve sensitivity of a bioassay or a biosensor. Although, much has been learned about the shape features and their effect on LSPR, many unanswered questions remain. A vast majority of research in the area of LSPR is currently focused on generating substrates that provide strong enhancements of the EM field and provide information on how manipulating physical parameters of NPs allows one to gain control over their optical properties. The polydispersity of NPs, particularly with wet synthesis methods, gives rise to broad absorption spectra hindering spectral resolution. Narrow bandwidth is commonly achieved with lithographic techniques, although typically at higher cost for manufacturing and smaller substrate sizes. The LSPR wavelength shift can be improved by either introducing a larger optical mass of analyte, or by incorporating a sandwich assay that either uses a chromophore with strong absorbance in the visible region allowing coupling with LSPR or by attaching another NP in layered format.

Interest in generation of “hot spots” by creation higher-order structures, such as nanostars, nanoflowers and nanocylinders is evident as lithographic techniques become more sophisticated. However, the primary limitation remains high reproducibility, which consequently impacts quantitative data analysis. Establishment of calibration curves remains a challenge in SERS applications. This issue is not just due to variability in the size of NPs, but also is associated with lack of control of the spatial positioning between NPs, between NP and reporter, the orientation of the biomolecule with respect to a “hot spot”, and non-specific adsorption. Nevertheless, SERS provides chemical information about analytes in close vicinity to a NP surface with high sensitivity and specificity.

Despite the challenges that LSPR faces in terms of implementation of practical applications, the scientific literature indicates that interest in assay development continues to grow at an exponential rate. LSPR provides rapid, easy and cost-effective experimental designs with at least comparable analytical performance. Despite the fact that the refractive index sensitivity is significantly greater for SPR, the decay length and therefore sensing volume is much smaller for LSPR. Additionally, LSPR allows for single nanoparticle detection and probing extremely small volumes. As a result, it provides potential for miniaturization of point-of-care and microfluidic devices. Further, LSPR can provide a platform for multiplexed analysis, which is crucial for clinical diagnostics and

proteomics. Introduction of SERS labels in a multiplexed assay may surpass the multiplexing capacity of fluorophores (1–3) and quantum dots (3–10) with the ability to incorporate 10–30 labels due to significantly small bandwidth of Raman peaks [143,191]. A further application is in the area of plasmonic “rulers” that can provide information about nanoscale distances which span over a wider range in comparison to FRET. The possibility of collecting three-dimensional time-dependent information about nanoscale motions and rearrangements has been illustrated in a proof-of-concept study using 3D rulers [192].

Acknowledgement

We are grateful to the Natural Sciences and Engineering Council of Canada for support of this research.

References

- [1] K.A. Willets, R.P. Van Duyne, *Annu. Rev. Phys. Chem.* 58 (2007) 267.
- [2] L.M. Liz-Marzan, *Langmuir* 22 (2006) 32.
- [3] X.M. Lu, M. Rycenga, S.E. Skrabalak, B. Wiley, Y.N. Xia, *Annu. Rev. Phys. Chem.* 60 (2009) 167.
- [4] T.R. Jensen, M.D. Malinsky, C.L. Haynes, R.P. Van Duyne, *J. Phys. Chem. B* 104 (2000) 10549.
- [5] J. Yguerabide, E.E. Yguerabide, *Anal. Biochem.* 262 (1998) 137.
- [6] J.N. Anker, W.P. Hall, O. Lyandres, N.C. Shah, J. Zhao, R.P. Van Duyne, *Nat. Mater.* 7 (2008) 442.
- [7] Y.H. Choi, T. Kang, L.P. Lee, *Nano Lett.* 9 (2009) 85.
- [8] Y. Choi, Y. Park, T. Kang, L.P. Lee, *Nat. Biotechnol.* 4 (2009) 742.
- [9] C.S. Thaxton, C.A. Mirkin, *Nat. Biotechnol.* 23 (2005) 681.
- [10] C. Sonnichsen, B.M. Reinhard, J. Liphardt, A.P. Alivisatos, *Nat. Biotechnol.* 23 (2005) 741.
- [11] A.J. Haes, R.P. Van Duyne, *Anal. Bioanal. Chem.* 379 (2004) 920.
- [12] S.A. Maier, H.A. Atwater, *J. Appl. Phys.* 98 (2005).
- [13] K.L. Kelly, E. Coronado, L.L. Zhao, G.C. Schatz, *J. Phys. Chem. B* 107 (2003) 668.
- [14] G.A. Ozin, A.C. Arsenault, L. Cademartini, *Nanochemistry: A Chemical Approach to Nanomaterials*, The Royal Society of Chemistry, Cambridge, 2009.
- [15] J. Perez-Juste, I. Pastoriza-Santos, L.M. Liz-Marzan, P. Mulvaney, *Coord. Chem. Rev.* 249 (2005) 1870.
- [16] S. Link, M.A. El-Sayed, *J. Phys. Chem. B* 103 (1999) 8410.
- [17] M. Hu, J.Y. Chen, Z.Y. Li, L. Au, G.V. Hartland, X.D. Li, M. Marquez, Y.N. Xia, *Chem. Soc. Rev.* 35 (2006) 1084.
- [18] A.E. Neeves, M.H. Birnboim, *J. Opt. Soc. Am. B Opt. Phys.* 6 (1989) 787.
- [19] B. Lee, I.M. Lee, S. Kim, D.H. Oh, L. Hesselink, *J. Modern Opt.* 57 (2010) 1479.
- [20] K. Vasilev, W. Knoll, M. Kreiter, *J. Chem. Phys.* 120 (2004) 3439.
- [21] P. Johansson, H.X. Xu, M. Kall, *Phys. Rev. B* 72 (2005).
- [22] B. Sepulveda, P.C. Angelome, L.M. Lechuga, L.M. Liz-Marzan, *Nano Today* 4 (2009) 244.
- [23] S.J. Lee, Z.Q. Guan, H.X. Xu, M. Moskovits, *J. Phys. Chem. C* 111 (2007) 17985.
- [24] K. Kneipp, Y. Wang, H. Kneipp, I. Itzkan, R.R. Dasari, M.S. Feld, *Phys. Rev. Lett.* 76 (1996) 2444.
- [25] T.L. Haslett, L. Tay, M. Moskovits, *J. Chem. Phys.* 113 (2000) 1641.
- [26] A.G. Brolo, A.C. Sanderson, A.P. Smith, *Phys. Rev. B* 69 (2004).
- [27] A.M. Michaels, J. Jiang, L. Brus, *J. Phys. Chem. B* 104 (2000) 11965.
- [28] J. Jiang, K. Bosnick, M. Maillard, L. Brus, *J. Phys. Chem. B* 107 (2003) 9964.
- [29] R.W. Taylor, T.C. Lee, O.A. Scherman, R. Esteban, J. Aizpurua, F.M. Huang, J.J. Baumberg, S. Mahajan, *ACS Nano* 5 (2011) 3878.
- [30] N. Harris, M.D. Arnold, M.G. Blaber, M.J. Ford, *J. Phys. Chem. C* 113 (2009) 2784.
- [31] J. Kneipp, H. Kneipp, M. McLaughlin, D. Brown, K. Kneipp, *Nano Lett.* 6 (2006) 2225.
- [32] G.R. Souza, C.S. Levin, A. Hajitou, R. Pasqualini, W. Arap, J.H. Miller, *Anal. Chem.* 78 (2006) 6232.
- [33] E.C. Le Ru, E. Blackie, M. Meyer, P.G. Etchegoin, *J. Phys. Chem. C* 111 (2007) 13794.
- [34] Y. Flegler, Y. Mastai, M. Rosenbluh, D.H. Dressler, *Surf. Sci.* 603 (2009) 788.
- [35] P.K. Jain, K.S. Lee, I.H. El-Sayed, M.A. El-Sayed, *J. Phys. Chem. B* 110 (2006) 7238.
- [36] A.D. McFarland, R.P. Van Duyne, *Nano Lett.* 3 (2003) 1057.
- [37] L.J. Sherry, R.C. Jin, C.A. Mirkin, G.C. Schatz, R.P. Van Duyne, *Nano Lett.* 6 (2006) 2060.
- [38] J. Gersten, A. Nitzan, *J. Chem. Phys.* 73 (1980) 3023.
- [39] T. Rindzevicius, Y. Alavertyan, A. Dahlin, F. Hook, D.S. Sutherland, M. Kall, *Nano Lett.* 5 (2005) 2335.
- [40] E.M. Larsson, J. Alegret, M. Kall, D.S. Sutherland, *Nano Lett.* 7 (2007) 1256.
- [41] X.Y. Zhang, E.M. Hicks, J. Zhao, G.C. Schatz, R.P. Van Duyne, *Nano Lett.* 5 (2005) 1503.
- [42] V.V. Tsukruk, H. Ko, S. Singamaneni, *Small* 4 (2008) 1576.
- [43] B. Lamprecht, G. Schider, R.T. Lechner, H. Ditlbacher, J.R. Krenn, A. Leitner, F.R. Aussenegg, *Phys. Rev. Lett.* 84 (2000) 4721.
- [44] M. Grzelczak, J. Perez-Juste, P. Mulvaney, L.M. Liz-Marzan, *Chem. Soc. Rev.* 37 (2008) 1783.
- [45] J. Zeng, X.H. Xia, M. Rycenga, P. Henneghan, Q.G. Li, Y.N. Xia, *Angew. Chem. Int. Ed.* 50 (2011) 244.
- [46] S.H. Chen, D.L. Carroll, *Nano Lett.* 2 (2002) 1003.
- [47] D.K. Smith, B.A. Korgel, *Langmuir* 24 (2008) 644.
- [48] I. Pastoriza-Santos, R.A. Alvarez-Puebla, L.M. Liz-Marzan, *Eur. J. Inorg. Chem.* (2010) 4288.
- [49] T.K. Sau, A.L. Rogach, *Adv. Mater.* 22 (2010) 1781.
- [50] J. Wilcoxon, *J. Phys. Chem. B* 113 (2009) 2647.
- [51] D. Aherne, D.M. Ledwith, J.M. Kelly, in: C.D. Geddes (Ed.), *Metal-Enhanced Fluorescence*, John Wiley & Sons, Inc., New Jersey, 2010, p. 295.
- [52] A.R. Tao, S. Habas, P.D. Yang, *Small* 4 (2008) 310.
- [53] J. Park, J. Joo, S.G. Kwon, Y. Jang, T. Hyeon, *Angew. Chem. Int. Ed.* 46 (2007) 4630.
- [54] C.J. Murphy, T.K. San, A.M. Gole, C.J. Orendorff, J.X. Gao, L. Gou, S.E. Hunyadi, T. Li, *J. Phys. Chem. B* 109 (2005) 13857.
- [55] S. Link, Z.L. Wang, M.A. El-Sayed, *J. Phys. Chem. B* 103 (1999) 3529.
- [56] A.N. Pisarenko, W.U. Spindel, R.T. Taylor, J.D. Brown, J.A. Cox, G.E. Pacey, *Talanta* 80 (2009) 777.
- [57] G. Gupta, D. Tanaka, Y. Ito, D. Shibata, M. Shimojo, K. Furuya, K. Mitsui, K. Kajikawa, *Nanotechnology* 20 (2009).
- [58] A. Boltasseva, *J. Opt. A Pure Appl. Opt.* 11 (2009).
- [59] W. Rechberger, A. Hohenau, A. Leitner, J.R. Krenn, B. Lamprecht, F.R. Aussenegg, *Opt. Commun.* 220 (2003) 137.
- [60] E. Hutter, J.H. Fendler, *Adv. Mater.* 16 (2004) 1685.
- [61] P.L. Stiles, J.A. Dieringer, N.C. Shah, R.R. Van Duyne, *Annu. Rev. Anal. Chem.* 1 (2008) 601.
- [62] A. Kosiorok, W. Kandulski, H. Glacyszynska, M. Giersig, *Small* 1 (2005) 439.
- [63] L.J. Guo, *Adv. Mater.* 19 (2007) 495.
- [64] J. Henzie, J. Lee, M.H. Lee, W. Hasan, T.W. Odom, *Annu. Rev. Phys. Chem.* 60 (2009) 147.
- [65] W. Wu, M. Hu, F.S. Ou, Z.Y. Li, R.S. Williams, *Nanotechnology* 21 (2010).
- [66] H.M. Bok, K.L. Shuford, S. Kim, S. KyuKim, S. Park, *Langmuir* 25 (2009) 5266.
- [67] A. Degiron, H.J. Lezec, N. Yamamoto, T.W. Ebbesen, *Opt. Commun.* 239 (2004) 61.
- [68] L. Stebounova, F. Chen, J. Bain, T.E. Schlesinger, S. Ip, G.C. Walker, *Appl. Opt.* 45 (2006) 6192.
- [69] W.A. Murray, S. Astilean, W.L. Barnes, *Phys. Rev. B* 69 (2004).
- [70] F. Chen, A. Itagi, J.A. Bain, D.D. Stancil, T.E. Schlesinger, L. Stebounova, G.C. Walker, B.B. Akhremitchev, *Appl. Phys. Lett.* 83 (2003) 3245.
- [71] J.Y. Xu, T.J. Xu, J. Wang, Q. Tian, *Opt. Eng.* 44 (2005).
- [72] A. Lesuffleur, L.K.S. Kumar, R. Gordon, *Appl. Phys. Lett.* 88 (2006).
- [73] K.J.K. Koerkamp, S. Enoch, F.B. Segerink, N.F. van Hulst, L. Kuipers, *Phys. Rev. Lett.* 92 (2004).
- [74] A. Degiron, T.W. Ebbesen, *J. Opt. A Pure Appl. Opt.* 7 (2005) S90.
- [75] K.L. van der Molen, F.B. Segerink, N.F. van Hulst, L. Kuipers, *Appl. Phys. Lett.* 85 (2004) 4316.
- [76] W.L. Barnes, A. Dereux, T.W. Ebbesen, *Nature* 424 (2003) 824.
- [77] A. Krishnan, T. Thio, T.J. Kim, H.J. Lezec, T.W. Ebbesen, P.A. Wolff, J. Pendry, L. Martin-Moreno, F.J. Garcia-Vidal, *Opt. Commun.* 200 (2001) 1.
- [78] A.G. Brolo, R. Gordon, B. Leathem, K.L. Kavanagh, *Langmuir* 20 (2004) 4813.
- [79] K. Shin, K.A. Leach, J.T. Goldbach, D.H. Kim, J.Y. Jho, M. Tuominen, C.J. Hawker, T.P. Russell, *Nano Lett.* 2 (2002) 933.
- [80] I. Ziler, J.E.F. Frost, V. Chabasseur-Molyneux, C.J.B. Ford, M. Pepper, *Semicond. Sci. Technol.* 11 (1996) 1235.
- [81] Y. Kobayashi, H. Katakami, E. Mine, D. Nagao, M. Konno, L.M. Liz-Marzan, *J. Colloid Interface Sci.* 283 (2005) 392.
- [82] D. Aherne, D.E. Charles, M.E. Brennan-Fournet, J.M. Kelly, Y.K. Gun'ko, *Langmuir* 25 (2009) 10165.
- [83] W.R. Algar, D.E. Prasuhn, M.H. Stewart, T.L. Jennings, J.B. Blanco-Canosa, P.E. Dawson, I.L. Medintz, *Bioconjug. Chem.* 22 (2011) 825.
- [84] N.T.K. Thanh, L.A.W. Green, *Nano Today* 5 (2010) 213.
- [85] S. Roh, T. Chung, B. Lee, *Sensors* 11 (2011) 1565.
- [86] M. Piliarik, H. Vaisocherova, J. Homola, *Methods Mol. Biol.* 503 (2009) 65.
- [87] L.J. Sherry, S.H. Chang, G.C. Schatz, R.P. Van Duyne, B.J. Wiley, Y.N. Xia, *Nano Lett.* 5 (2005) 2034.
- [88] H. Wang, D.W. Brandl, F. Le, P. Nordlander, N.J. Halas, *Nano Lett.* 6 (2006) 827.
- [89] B. Luk'yanchuk, N.I. Zheludev, S.A. Maier, N.J. Halas, P. Nordlander, H. Giessen, C.T. Chong, *Nat. Mater.* 9 (2010) 707.
- [90] N.J. Halas, S. Lal, W.S. Chang, S. Link, P. Nordlander, *Chem. Rev.* 111 (2011) 3913.
- [91] N. Verellen, P. Van Dorpe, C.J. Huang, K. Lodewijks, G.A.E. Vandenbosch, L. Lagae, V.V. Moshchalkov, *Nano Lett.* 11 (2011) 391.
- [92] N. Nath, A. Chilkoti, *Anal. Chem.* 76 (2004) 5370.
- [93] K. Fujiwara, H. Watarai, H. Itoh, E. Nakahama, N. Ogawa, *Anal. Bioanal. Chem.* 386 (2006) 639.
- [94] M.P. Kreuzer, R. Quidant, J.P. Salazar, M.P. Marco, G. Badenes, *Anal. Bioanal. Chem.* 391 (2008) 1813.
- [95] S.M. Marinakos, S. Chen, A. Chilkoti, *Anal. Chem.* 79 (2007) 5278.
- [96] G.J. Nusz, S.M. Marinakos, A.C. Curry, A. Dahlin, F. Hook, A. Wax, A. Chilkoti, *Anal. Chem.* 80 (2008) 984.
- [97] C. Wang, J. Irudayaraj, *Small* 4 (2008) 2204.
- [98] C.X. Yu, J. Irudayaraj, *Anal. Chem.* 79 (2007) 572.
- [99] P.K. Jain, M.A. El-Sayed, *J. Phys. Chem. C* 111 (2007) 17451.
- [100] Y.G. Sun, Y.N. Xia, *Anal. Chem.* 74 (2002) 5297.
- [101] C.R. Yonzon, E. Jeoung, S.L. Zou, G.C. Schatz, M. Mrksich, R.P. Van Duyne, *J. Am. Chem. Soc.* 126 (2004) 12669.

- [102] A.J. Haes, W.P. Hall, L. Chang, W.L. Klein, R.P. Van Duyne, *Nano Lett.* 4 (2004) 1029.
- [103] A.J. Haes, L. Chang, W.L. Klein, R.P. Van Duyne, *J. Am. Chem. Soc.* 127 (2005) 2264.
- [104] R.P. Van Duyne, W.P. Hall, S.N. Ngatia, *J. Phys. Chem. C* 115 (2011) 1410.
- [105] Y.B. Lin, Y. Zou, Y.Y. Mo, J.P. Guo, R.G. Lindquist, *Sensors* 10 (2010) 9397.
- [106] J. Zhao, A. Das, X.Y. Zhang, G.C. Schatz, S.G. Sligar, R.P. Van Duyne, *J. Am. Chem. Soc.* 128 (2006) 11004.
- [107] J. Ferreira, M.J.L. Santos, M.M. Rahman, A.G. Brolo, R. Gordon, D. Sinton, E.M. Girotto, *J. Am. Chem. Soc.* 131 (2009) 436.
- [108] J.C. Sharpe, J.S. Mitchell, L. Lin, H. Sedoglavich, R.J. Blaikie, *Anal. Chem.* 80 (2008) 2244.
- [109] T. Endo, K. Kerman, N. Nagatani, H.M. Hiepa, D.K. Kim, Y. Yonezawa, K. Nakano, E. Tamiya, *Anal. Chem.* 78 (2006) 6465.
- [110] H.M. Hiep, T. Nakayama, M. Saito, S. Yamamura, Y. Takamura, E. Tamiya, *Jpn. J. Appl. Phys.* 47 (2008) 1337.
- [111] C.J. Huang, K. Bonroy, G. Reekman, K. Verstreken, L. Lagae, G. Borghs, *Microelectron. Eng.* 86 (2009) 2437.
- [112] P.K. Jain, X.H. Huang, I.H. El-Sayed, M.A. El-Sayed, *Acc. Chem. Res.* 41 (2008) 1578.
- [113] G.L. Liu, Y.D. Yin, S. Kunchakarra, B. Mukherjee, D. Gerion, S.D. Jett, D.G. Bear, J.W. Gray, A.P. Alivisatos, L.P. Lee, F.Q.F. Chen, *Nat. Nanotechnol.* 1 (2006) 47.
- [114] G.L. Liu, Y.T. Long, Y. Choi, T. Kang, L.P. Lee, *Nat. Methods* 4 (2007) 1015.
- [115] O. Lyandres, N.C. Shah, C.R. Yonzon, J.T. Walsh, M.R. Glucksberg, R.P. Van Duyne, *Anal. Chem.* 77 (2005) 6134.
- [116] D.A. Stuart, C.R. Yonzon, X.Y. Zhang, O. Lyandres, N.C. Shah, M.R. Glucksberg, J.T. Walsh, R.P. Van Duyne, *Anal. Chem.* 77 (2005) 4013.
- [117] N.C. Shah, O. Lyandres, J.T. Walsh, M.R. Glucksberg, R.P. Van Duyne, *Anal. Chem.* 79 (2007) 6927.
- [118] X.Y. Zhang, M.A. Young, O. Lyandres, R.P. Van Duyne, *J. Am. Chem. Soc.* 127 (2005) 4484.
- [119] X.Y. Zhang, J. Zhao, A.V. Whitney, J.W. Elam, R.P. Van Duyne, *J. Am. Chem. Soc.* 128 (2006) 10304.
- [120] D.A. Stuart, K.B. Biggs, R.P. Van Duyne, *Analyst* 131 (2006) 568.
- [121] D. Li, D.W. Li, J.S. Fossey, Y.T. Long, *Anal. Chem.* 82 (2010) 9299.
- [122] D.A. Stuart, J.M. Yuen, N.S.O. Lyandres, C.R. Yonzon, M.R. Glucksberg, J.T. Walsh, R.P. Van Duyne, *Anal. Chem.* 78 (2006) 7211.
- [123] U. Utzinger, D.L. Heintzelman, A. Mahadevan-Jansen, A. Malpica, M. Follen, R. Richards-Kortum, *Appl. Spectrosc.* 55 (2001) 955.
- [124] Y.S. Huh, A.J. Chung, B. Cordovez, D. Erickson, *Lab. Chip* 9 (2009) 433.
- [125] W. Yuan, H.P. Ho, R.K.Y. Lee, S.K. Kong, *Appl. Opt.* 48 (2009) 4329.
- [126] T. Vo-Dinh, *IEEE J. Sel. Top. Quantum Electron.* 14 (2008) 198.
- [127] M.B. Wabuyele, T. Vo-Dinh, *Anal. Chem.* 77 (2005) 7810.
- [128] L. Fabris, M. Dante, G. Braun, S.J. Lee, N.O. Reich, M. Moskovits, T.Q. Nguyen, G.C. Bazan, *J. Am. Chem. Soc.* 129 (2007) 6086.
- [129] I. Pavel, E. McCarney, A. Elkhalel, A. Morrill, K. Plaxco, M. Moskovits, *J. Phys. Chem. C* 112 (2008) 4880.
- [130] R.C. Maher, S.A. Maier, L.F. Cohen, L. Koh, A. Laromaine, J.A.G. Dick, M.M. Stevens, *J. Phys. Chem. C* 114 (2010) 7231.
- [131] A.R. Bizzarri, S. Cannistraro, *Nanomed. Nanotechnol. Biol. Med.* 3 (2007) 306.
- [132] T. Li, L.P. Guo, Z. Wang, *Anal. Sci.* 24 (2008) 907.
- [133] Z. Chen, S.M. Tabakman, A.P. Goodwin, M.G. Kattah, D. Daranciang, X.R. Wang, G.Y. Zhang, X.L. Li, Z. Liu, P.J. Utz, K.L. Jiang, S.S. Fan, H.J. Dai, *Nat. Biotechnol.* 26 (2008) 1285.
- [134] M.D. Porter, R.J. Lipert, L.M. Siperko, G. Wang, R. Narayananana, *Chem. Soc. Rev.* 37 (2008) 1001.
- [135] M. Gellner, B. Kustner, S. Schlucker, *Vib. Spectrosc.* 50 (2009) 43.
- [136] S.P. Mulvaney, M.D. Musick, C.D. Keating, M.J. Natan, *Langmuir* 19 (2003) 4784.
- [137] W.E. Doering, S.M. Nie, *Anal. Chem.* 75 (2003) 6171.
- [138] W.E. Doering, M.E. Piotti, M.J. Natan, R.G. Freeman, *Adv. Mater.* 19 (2007) 3100.
- [139] M.X. Yang, T. Chen, W.S. Lau, Y. Wang, Q.H. Tang, Y.H. Yang, H.Y. Chen, *Small* 5 (2009) 198.
- [140] X. Su, J. Zhang, L. Sun, T.W. Koo, S. Chan, N. Sundararajan, M. Yamakawa, A.A. Berlin, *Nano Lett.* 5 (2005) 49.
- [141] D. Graham, K. Faulds, W.E. Smith, *Chem. Commun.* (2006) 4363.
- [142] Y.C. Cao, R.C. Jin, J.M. Nam, C.S. Thaxton, C.A. Mirkin, *J. Am. Chem. Soc.* 125 (2003) 14676.
- [143] D.S. Grubisha, R.J. Lipert, H.Y. Park, J. Driskell, M.D. Porter, *Anal. Chem.* 75 (2003) 5936.
- [144] Y.W.C. Cao, R.C. Jin, C.A. Mirkin, *Science* 297 (2002) 1536.
- [145] X.H. Huang, P.K. Jain, I.H. El-Sayed, M.A. El-Sayed, *Lasers Med. Sci.* 23 (2008) 217.
- [146] G. Breuzard, J.F. Angiboust, P. Jeannesson, M. Manfait, J.M. Millot, *Biochem. Biophys. Res. Commun.* 320 (2004) 615.
- [147] K. Kneipp, H. Kneipp, J. Kneipp, *Acc. Chem. Res.* 39 (2006) 443.
- [148] S. Balint, S. Rao, M.M. Sanchez, V. Huntuosova, P. Miskovsky, D. Petrov, *J. Biomed. Opt.* 15 (2010).
- [149] A. Shamsaie, M. Jonczyk, J. Sturgis, J.P. Robinson, J. Irudayaraj, *J. Biomed. Opt.* 12 (2007).
- [150] M.K. Gregas, J.P. Scaffidi, B. Lauly, T. Vo-Dinh, *Appl. Spectrosc.* 64 (2010) 858.
- [151] J.Q. Lin, R. Chen, S.Y. Feng, Y.Z. Li, Z.F. Huang, S.S. Xie, Y. Yu, M. Cheng, H.S. Zeng, *Biosens. Bioelectron.* 25 (2009) 388.
- [152] M.Y. Sha, H.X. Xu, M.J. Natan, R. Cromer, *J. Am. Chem. Soc.* 130 (2008) 17214.
- [153] X.M. Qian, X.H. Peng, D.O. Ansari, Q. Yin-Goen, G.Z. Chen, D.M. Shin, L. Yang, A.N. Young, M.D. Wang, S.M. Nie, *Nat. Biotechnol.* 26 (2008) 83.
- [154] C.D. Geddes, K. Aslan, S.N. Malyn, *Analyst* 132 (2007) 1112.
- [155] D.D. Evanoff, G. Chumanov, *Chemphyschem* 6 (2005) 1221.
- [156] K. Munechika, Y. Chen, A.F. Tillack, A.P. Kulkarni, I.J.L. Plante, A.M. Munro, D.S. Ginger, *Nano Lett.* 10 (2010) 2598.
- [157] Y. Chen, K. Munechika, D.S. Ginger, *Nano Lett.* 7 (2007) 690.
- [158] P. Bharadwaj, L. Novotny, *Opt. Express* 15 (2007) 14266.
- [159] Y.C. Chen, K. Munechika, I. Jen-La Plante, A.M. Munro, S.E. Skrabalak, Y.N. Xia, D.S. Ginger, *Appl. Phys. Lett.* 93 (2008).
- [160] K. Munechika, Y. Chen, A.F. Tillack, A.P. Kulkarni, I. Jen-La Plante, A.M. Munro, D.S. Ginger, *Nano Lett.* 11 (2011) 2725.
- [161] K. Ray, R. Badugu, J.R. Lakowicz, *J. Phys. Chem. C* 111 (2007) 7091.
- [162] K. Ray, R. Badugu, J.R. Lakowicz, *Chem. Mater.* 19 (2007) 5902.
- [163] K. Aslan, I. Gryczynski, J. Malicka, E. Matveeva, J.R. Lakowicz, C.D. Geddes, *Curr. Opin. Biotechnol.* 16 (2005) 55.
- [164] C.D. Geddes, J.R. Lakowicz, *J. Fluoresc.* 12 (2002) 121.
- [165] J.R. Lakowicz, J. Malicka, S. D'Auria, I. Gryczynski, *Anal. Biochem.* 320 (2003) 13.
- [166] J. Malicka, I. Gryczynski, J.Y. Fang, J.R. Lakowicz, *Anal. Biochem.* 317 (2003) 136.
- [167] J. Malicka, I. Gryczynski, Z. Gryczynski, J.R. Lakowicz, *Anal. Biochem.* 315 (2003) 57.
- [168] J.G.L.L. Malicka Jr., *Anal. Chem.* 75 (2003) 4408.
- [169] J.D. Batteas, Y.H. Chan, J.X. Chen, Q.S. Liu, S.E. Wark, D.H. Son, *Anal. Chem.* 82 (2010) 3671.
- [170] S. Ekgasit, C. Thammacharoen, F. Yu, W. Knoll, *Anal. Chem.* 76 (2004) 2210.
- [171] K. Aslan, J. Huang, G.M. Wilson, C.D. Geddes, *J. Am. Chem. Soc.* 128 (2006) 4206.
- [172] K. Aslan, T.A.J. Grell, *Clin. Chem.* 57 (2011) 746.
- [173] C.D. Geddes, N. Bondre, Y.X. Zhang, *Sens. Actuators A* 152 (2011) 82.
- [174] E. Matveeva, Z. Gryczynski, J. Malicka, I. Gryczynski, J.R. Lakowicz, *Anal. Biochem.* 334 (2004) 303.
- [175] K. Aslan, P. Holley, C.D. Geddes, *J. Immunol. Methods* 312 (2006) 137.
- [176] Y.D. Zhao, Y.Q. Li, L.Y. Guan, H.L. Zhang, J. Chen, S. Lin, Z.Y. Ma, *Anal. Chem.* 83 (2011) 4103.
- [177] K. Aslan, Z. Leonenko, J.R. Lakowicz, C.D. Geddes, *J. Phys. Chem. B* 109 (2005) 3157.
- [178] Y. Fu, J. Zhang, J.R. Lakowicz, *J. Am. Chem. Soc.* 132 (2010) 5540.
- [179] P.P. Pompa, L. Martiradonna, A. Della Torre, F. Della Sala, L. Manna, M. De Vittorio, F. Calabi, R. Cingolani, R. Rinaldi, *Nat. Nanotechnol.* 1 (2006) 126.
- [180] K. Aslan, Z. Leonenko, J.R. Lakowicz, C.D. Geddes, *J. Fluoresc.* 15 (2005) 643.
- [181] J.R. Lakowicz, J. Malicka, I. Gryczynski, *Biotechniques* 34 (2003) 62.
- [182] C.R. Sabanayagam, J.R. Lakowicz, *Nucleic Acids Res.* 35 (2007).
- [183] K. Aslan, C.D. Geddes, in: C.D. Geddes (Ed.), *Metal-Enhanced Fluorescence*, John Wiley & Sons, Inc., Hoboken, NJ, 2010.
- [184] K. Aslan, C.D. Geddes, *Anal. Chem.* 77 (2005) 8057.
- [185] K. Aslan, J.R. Lakowicz, C.D. Geddes, *Abstr. Papers Am. Chem. Soc.* 230 (2005) U1208.
- [186] C.D. Geddes, K. Aslan, S.N. Malyn, *Biochem. Biophys. Res. Commun.* 348 (2006) 612.
- [187] C.D. Geddes, K. Aslan, M.J.R. Previte, Y.X. Zhang, T. Gallagher, L. Baillie, *Anal. Chem.* 80 (2008) 4125.
- [188] C.D. Geddes, A.D. Dragan, A.I.K. Golberg, A. Elbaz, R. Marks, Y.X. Zhang, *J. Immunol. Methods* 366 (2011) 1.
- [189] K. Aslan, *Nano Biomed. Eng.* 2 (2010) 1.
- [190] S.M. Tennant, Y.X. Zhang, J.E. Galen, C.D. Geddes, M.M. Levine, *PLoS One* 6 (2011).
- [191] S. Schlucker, *Chemphyschem* 10 (2009) 1344.
- [192] N. Liu, M. Hentschel, T. Weiss, A.P. Alivisatos, H. Giessen, *Science* 332 (2011) 1407.
- [193] N. Nath, A. Chilkoti, *Anal. Chem.* 74 (2002) 504.
- [194] J.F. Wang, H.J. Chen, X.S. Kou, Z. Yang, W.H. Ni, *Langmuir* 24 (2008) 5233.
- [195] F. Tam, C. Moran, N.J. Halas, *J. Phys. Chem. B* 108 (2004) 17290.
- [196] C.L. Nehl, H.W. Liao, J.H. Hafner, *Nano Lett.* 6 (2006) 683.
- [197] H. Giessen, N. Liu, T. Weiss, M. Mesch, L. Langguth, U. Eigenthaler, M. Hirscher, C. Sonnichsen, *Nano Lett.* 10 (2010) 1103.
- [198] J.J. Mock, D.R. Smith, S. Schultz, *Nano Lett.* 3 (2003) 485.
- [199] G.C. Schatz, L.J. Sherry, R.C. Jin, C.A. Mirkin, R.P. Van Duyne, *Nano Lett.* 6 (2006) 2060.
- [200] M.D. Malinsky, K.L. Kelly, G.C. Schatz, R.P. Van Duyne, *J. Am. Chem. Soc.* 123 (2001) 1471.
- [201] E.C. Le Ru, P.G. Etchegoin, *Phys. Chem. Chem. Phys.* 10 (2008) 6079.